19. Walter, F., Murchie, A. I., Duckett, D. R. & Lilley, D. M. Global structure of four-way RNA junctions studied using fluorescence resonance energy transfer. *RNA* **4**, 719–728 (1998).

20. Liautard, J. -P., Sri-Widada, J., Brunel, C. & Jeanteur, P. Structural organisation of ribonucleoproteins containing small nuclear RNAs from HeLa cells. *J. Mol. Biol.* **162**, 623–643 (1982).

21. Hartmuth, K., Raker, V. A., Huber, J., Branlant, C. & Lührmann, R. An unusual chemical reactivity of Sm site adenosines strongly correlates with proper assembly of core U snRNP particles. *J. Mol. Biol.* **285**, 133–147 (1999).

22. Hoet, R. M., Kastner, B., Lührmann, R. & van Venrooij, W. J. Purification and characterization of human autoantibodies directed to specific regions on U1RNA; recognition of native U1RNP complexes. *Nucleic Acids Res.* **21**, 5130–5136 (1993).

23. Lin, W. -L. & Pederson, T. Ribonucleoprotein organization of eukaryotic RNA. XXXI. Structure of the U1 small nuclear ribonucleoprotein. *J. Mol. Biol.* **180**, 947–960 (1984).

24. Urlaub, H., Raker, V., Kostka, S. & Lührmann, R. Sm protein–Sm site RNA interactions within the inner ring of the spliceosomal snRNP core structure. *EMBO J.* **20**, 1–10 (2001).

25. Heinrichs, V., Bach, M., Winckelmann, G. & Lührmann, R. U1-specific protein C needed for efficient complex formation of U1 snRNP with a 5′ splice site. *Science* **247**, 69–72 (1990).

26. Adrian, M., Dubochet, J., Lepault, J. & McDowall, A. W. Cryo-electron microscopy of viruses. *Nature* **308**, 32–36 (1984).

27. van Heel, M., Harauz, G. & Orlova, E. V. A new generation of the IMAGIC image processing system. *J. Struct. Biol.* **116**, 17–24 (1996).

28. van Heel, M. & Frank, J. Use of multivariate statistics in analysing the images of biological macromolecules. *Ultramicroscopy* **6**, 187–194 (1981).

29. van Heel, M. & Harauz, G. Resolution criteria for three-dimensional reconstruction. *Optik* **73**, 119–122 (1986).

••

addendum

A one-hit model of cell death in inherited neuronal degenerations

G. Clarke, R. A. Collins, B. R. Leavitt, D. F. Andrews, M. R. Hayden, C. J. Lumsden & R. R. McInnes

Nature **406**, 195–199 (2000).

It has been questioned whether our neurodegeneration model was anticipated by Calne and co-workers[1–4]. Both groups related exponential neuronal loss to pathogenesis, but the models are radically different. We recognized that in neurodegeneration, exponential death kinetics mean that the risk of cell death remains constant with age. To accommodate constant risk, we proposed a one-hit model: the hit is a *consequence* of a neuron being in a high-risk (for example, mutant) state; a hit is a biochemical reaction within each *single* neuron, committing it to death at a random time. We noted that constant risk excludes cumulative intracellular damage as a disease mechanism.

Calne *et al.* proposed that in idiopathic Parkinsonism "An event [for example, infection] acts on the neuronal *population* over a brief period …[to initiate disease]"[2]. They excluded ongoing processes as causing idiopathic Parkinsonism[2,4], but the role of cumulative intracellular damage was not addressed. Their focus on whole neuron populations and on events that act on them is notable, and complementary to but different from our model. □

1. Lee, C. S. *et al.* Clinical observations on the rate of progression of idiopathic parkinsonism. *Brain* **117**, 501–507 (1994).

2. Schulzer, M., Lee, C. S., Mak, E. K., Vingerhoets, F. J. G. & Calne, D. B. A mathematical model of pathogenesis in idiopathic parkinsonism. *Brain* **117**, 509–516 (1994).

3. Calne, D. B. Is idiopathic parkinsonism the consequence of an event or a process? *Neurology* **44**, 5–10 (1994).

4. Lee, C. S. *et al.* Patterns of asymmetry do not change over the course of idiopathic parkinsonism: implications for pathogenesis. *Neurology* **45**, 435–439 (1995).

corrections

Kainate receptors are involved in synaptic plasticity

Zuner A. Bortolotto, Vernon R. J. Clarke, Caroline M. Delany, Michael C. Parry, Ilse Smolders, Michel Vignes, Ken H. Ho, Peter Miu, Bradford T. Brinton, Robert Fantaske, Ann Ogden, Mary Gates, Paul L. Ornstein, David Lodge, David Bleakman & Graham L. Collingridge

Nature **402**, 297–301 (1999).

In this paper, the authors omitted the reference to the published synthetic pathway[1] by which the selective GluR5 kainate receptor antagonist LY382884 may be made. □

1. Bleisch, T. J. *et al.* Structure activity studies of aryl-spaced decahydroisoquinoline-3-carboxylic acid AMPA receptor antagonists. *Bioorg. Med. Chem. Lett.* **7**, 1161–1166 (1997).

Error and attack tolerance of complex networks

Réka Albert, Hawoong Jeong & Albert-László Barabasi

Nature **406**, 378–382 (2000).

In this paper, the error tolerance curves for the exponential network were affected by a software error. This did not impact the attack curves nor the measurements and conclusions regarding the error/attack tolerance of scale-free networks, the World-Wide Web and the Internet. The corrected Figs 2a and 3a are shown below. □
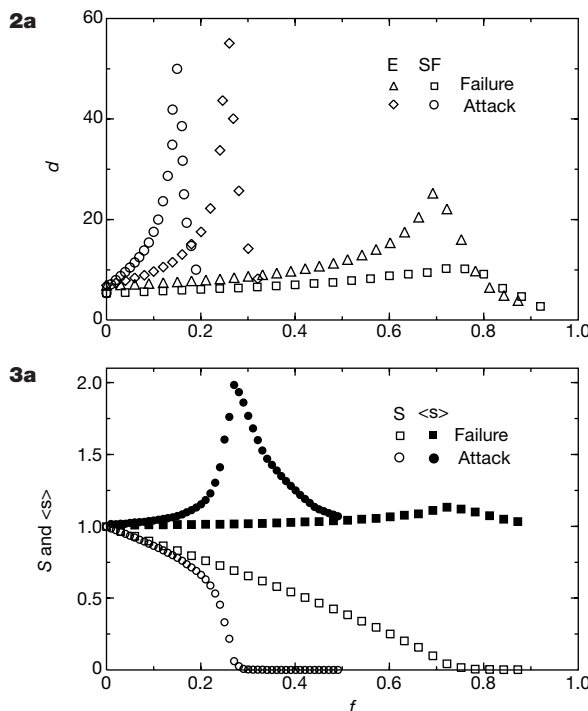
not elicit any Ca^{2+} response (data not shown). To measure MAP kinase activation, pEF6–*mil*, pEF6–*mil*^{m93} or pEF6–*mil*^{te273} were transiently co-tranfected with a reporter activated by MAP kinase-stimulated Elk-1 (Stratagene) into Jurkat T cells. Normalization of transfection was performed with a pCMV-Renilla luciferase construct and the Stop&Glo reagent (Promega). After stimulation with 100 nM S1P for 4 h, activities of the Firefly and Renilla luciferases were measured in cell lysates. The C305 anti-T-cell receptor antibody gave similar Ca^{2+} and MAP kinase responses in all transfectants.

Phenotypic rescue and genotyping

For RNA injections, the *mil* construct was generated by PCR using wild-type cDNA and cloned into pCS2+. Injected embryos were genotyped using allele-specific restriction fragment length polymorphisms.

1. Chen, J. N. *et al.* Mutations affecting the cardiovascular system and other internal organs in zebrafish. *Development* **123**, 293–302 (1996).
2. Stainier, D. Y. R. *et al.* Mutations affecting the formation and function of the cardiovascular system in the zebrafish embryo. *Development* **123**, 285–92 (1996).
3. Yelon, D. *et al.* The bHLH transcription factor Hand2 plays parallel roles in zebrafish heart and pectoral fin development. *Development* **127**, 2573–2582 (2000).
4. Yelon, D., Horne, S. & Stainier, D. Y. R. Restricted expression of cardiac myosin genes reveals regulated aspects of heart tube assembly in zebrafish. *Dev. Biol.* **214**, 23–37 (1999).
5. Kikuchi, Y. *et al.* The zebrafish *bonnie and clyde* gene encodes a Mix family homeodomain protein that regulates the generation of endodermal precursors. *Genes Dev.* **14**, 1279–1289 (2000).
6. Reiter, J. F. *et al.* Gata5 is required for the development of the heart and endoderm in zebrafish. *Genes Dev.* **13**, 2983–2995 (1999).
7. Schier, A. F., Neuhauss, S. C., Helde, K. A., Talbot, W. S. & Driever, W. The *one-eyed pinhead* gene functions in mesoderm and endoderm formation in zebrafish and interacts with *no tail*. *Development* **124**, 327–342 (1997).
8. Alexander, J., Rothenberg, M., Henry, G. L. & Stainier, D. Y. R. *casanova* plays an early and essential role in endoderm formation in zebrafish. *Dev. Biol.* **215**, 343–357 (1999).
9. Alexander, J. & Stainier, D. Y. R. *Mutations affecting cardiac development in zebrafish* (eds. Harvey, R. & Rosenthal, N.) (Academic, San Diego, 1999).
10. Strähle, U., Blader, P., Henrique, D. & Ingham, P. W. *axial*, a zebrafish gene expressed along the developing body axis, shows altered expression in *cyclops* mutant embryos. *Genes Dev.* **7**, 1436–1446 (1993).
11. Knapik, E. W. *et al.* A microsatellite genetic linkage map for zebrafish (Danio rerio). *Nature Genet.* **18**, 338–343 (1998).
12. Chan, F. Y. *et al.* Characterization of adult alpha- and beta-globin genes in the zebrafish. *Blood* **89**, 688–700 (1997).
13. Martin, C. C., Laforest, L., Akimenko, M. A. & Ekker, M. A role for DNA methylation in gastrulation and somite patterning. *Dev. Biol.* **206**, 189–205 (1999).
14. Okazaki, H. *et al.* Molecular cloning of a novel putative G protein-coupled receptor expressed in the cardiovascular system. *Biochem. Biophys. Res. Commun.* **190**, 1104–1109 (1993).
15. An, S. *et al.* Identification of cDNAs encoding two G protein-coupled receptors for lysosphingolipids. *FEBS Lett.* **417**, 279–282 (1997).
16. MacLennan, A. J., Browe, C. S., Gaskin, A. A., Lado, D. C. & Shaw, G. Cloning and characterization of a putative G-protein coupled receptor potentially involved in development. *Mol. Cell. Neurosci.* **5**, 201–209 (1994).
17. An, S., Bleu, T. & Zheng, Y. Transduction of intracellular calcium signals through G protein-mediated activation of phospholipase C by recombinant sphingosine 1-phosphate receptors. *Mol. Pharmacol.* **55**, 787–794 (1999).
18. Goetzl, E. J. & An, S. Diversity of cellular receptors and functions for the lysophospholipid growth factors lysophosphatidic acid and sphingosine 1-phosphate. *FASEB J.* **12**, 1589–1598 (1998).
19. An, S., Zheng, Y. & Bleu, T. Sphingosine 1-phosphate-induced cell proliferation, survival, and related signaling events mediated by G protein-coupled receptors Edg3 and Edg5. *J. Biol. Chem.* **275**, 288–296 (2000).
20. Lee, M. J. *et al.* Sphingosine-1-phosphate as a ligand for the G protein-coupled receptor EDG-1. *Science* **279**, 1552–1555 (1998).
21. Forbes, A. & Lehmann, R. Cell migration in *Drosophila*. *Curr. Opin. Genet. Dev.* **9**, 473–478 (1999).
22. Zhang, N., Zhang, J., Purcell, K. J., Cheng, Y. & Howard, K. The *Drosophila* protein Wunen repels migrating germ cells. *Nature* **385**, 64–67 (1997).
23. Roberts, R., Sciorra, V. A. & Morris, A. J. Human type 2 phosphatidic acid phosphohydrolases. Substrate specificity of the type 2a, 2b, and 2c enzymes and cell surface activity of the 2a isoform. *J. Biol. Chem.* **273**, 22059–22067 (1998).
24. Scheer, A. *et al.* Mutational analysis of the highly conserved arginine within the glu/asp-arg-tyr motif of the α_{1b}-adrenergic receptor: effects on receptor isomerization and activation. *Mol. Pharmacol.* **57**, 219—231 (2000).
25. Strader, C. D., Fong, T. M., Tota, M. R., Underwood, D. & Dixon, R. A. Structure and function of G protein-coupled receptors. *Annu. Rev. Biochem.* **63**, 101–132 (1994).
26. Hla, T. *et al.* Sphingosine-1-phosphate: extracellular mediator or intracellular second messenger? *Biochem. Pharmacol.* **58**, 201–207 (1999).
27. Spiegel, S. Sphingosine 1-phosphate: a prototype of a new class of second messengers. *J. Leukocyte Biol.* **65**, 341–344 (1999).
28. Moolenaar, W. H. Bioactive lysophospholipids and their G protein-coupled receptors. *Exp. Cell Res.* **253**, 230–238 (1999).

Supplementary information is available on *Nature*'s World-Wide Web site (http://www.nature.com) or as paper copy from the London editorial office of *Nature*.

....

A one-hit model of cell death in inherited neuronal degenerations

Geoff Clarke*†, **Richard A. Collins**†, **Blair R. Leavitt**‡, **David F. Andrews**§, **Michael R. Hayden**‡, **Charles J. Lumsden**|| & **Roderick R. McInnes***†||¶

* *Programs in Developmental Biology and Genetics, The Research Institute, Hospital for Sick Children, 555 University Ave., Toronto, Ontario M5G 1X8, Canada*
† *Departments of Molecular and Medical Genetics, ¶ Pediatrics, and || Department of Medicine, Institute of Medical Science, University of Toronto, 1 King's College Circle, Toronto, Ontario M5S 1A8, Canada*
‡ *Centre for Molecular Medicine and Therapeutics, Department of Medical Genetics University of British Columbia, Vancouver, British Columbia V5Z 4H4, Canada*
§ *Department of Statistics, University of Toronto, 100 St. George Street, M5S 3G3, Canada*

....

In genetic disorders associated with premature neuronal death, symptoms may not appear for years or decades. This delay in clinical onset is often assumed to reflect the occurrence of age-dependent cumulative damage[1–6]. For example, it has been suggested that oxidative stress disrupts metabolism in neurological degenerative disorders by the cumulative damage of essential macromolecules[1,4,7]. A prediction of the cumulative damage hypothesis is that the probability of cell death will increase over time. Here we show in contrast that the kinetics of neuronal death in 12 models of photoreceptor degeneration, hippocampal neurons undergoing excitotoxic cell death[8], a mouse model of cerebellar degeneration[9] and Parkinson's[10] and Huntington's diseases are all exponential and better explained by mathematical models in which the risk of cell death remains constant or decreases exponentially with age. These kinetics argue against the cumulative damage hypothesis; instead, the time of death of any neuron is random. Our findings are most simply accommodated by a 'one-hit' biochemical model in which mutation imposes a mutant steady state on the neuron and a single event randomly initiates cell death. This model appears to be common to many forms of neurodegeneration and has implications for therapeutic strategies.

To distinguish between the increasing risk of death associated with cumulative damage (which would generate a sigmoidal decline in cell number) and the exponential decline in cell number that results from a constant or decreasing risk of death (Fig. 1a), we used regression analysis to analyse photoreceptor neuron death in 11 animal models of inherited retinal degeneration and an experimental model of retinal detachment. These models include animals with mutations in genes encoding a range of proteins including the photosensitive pigment rhodopsin (M. M. LaVail, personal communication), the enzyme cyclic GMP phosphodiesterase[11,12] and the structural proteins rom-1 (ref. 13) and peripherin/rds[14,15]. In three other mutants analysed, the affected gene is unknown.

In five of these examples (Fig. 1, Table 1, and see Supplementary Information), the data fit only to mathematical models in which the probability of photoreceptor death remains constant with age. In six

others (Fig. 2, Table 1), the kinetics fit equally well to models of constant or exponentially decreasing risk of death. Consequently, in all of these animal models the increasing risk of photoreceptor death predicted by the cumulative damage hypothesis can be excluded, a possible exception being the $Rd^{-/-}$ mouse in which the data (Fig. 1d) fit equally well to models of constant ($R^2 = 0.985$, $P < 0.001$) and exponentially increasing risk ($R^2 = 0.980$; $P < 0.001$). Thus, even if age-dependent cumulative damage does occur in these mutant retinas, it is not associated with an increase in the probability that the photoreceptors will die.

In agreement with these direct measurements of the kinetics of photoreceptor death in animal models, clinical assessment of photoreceptor function in patients with retinitis pigmentosa and cone-rod dystrophy has shown that both visual field loss[16] and the decay of the maximum photoreceptor electroretinogram responses also observe exponential kinetics[17,18]. Thus, the exponen-

tial cell death kinetics that we have identified in animal models appear to be shared by most, if not all, examples of inherited retinal degeneration.

To determine whether a constant or exponentially decreasing risk of neuronal death is a general phenomenon shared by other classes of neuron, we examined the kinetics of neurodegeneration in four other diseases or experimental models. Neuronal loss in the substantia nigra in Parkinson's disease[10], the excitotoxic death of cultured hippocampal neurons[8] and the loss of cerebellar granule cells in *pcd/pcd* (Purkinje cell degeneration) mice[9] have been shown to produce an exponential decline in neuronal number with time. Our regression analyses demonstrate that only a constant risk describes the kinetics of cell death in the first two of these examples (Table 1, Fig. 3a, b). On the other hand, the loss of cerebellar granule cells subsequent to the genetically determined loss of their target Purkinje neurons in *pcd/pcd* mice[9] (Fig. 3c) and neuronal death in a
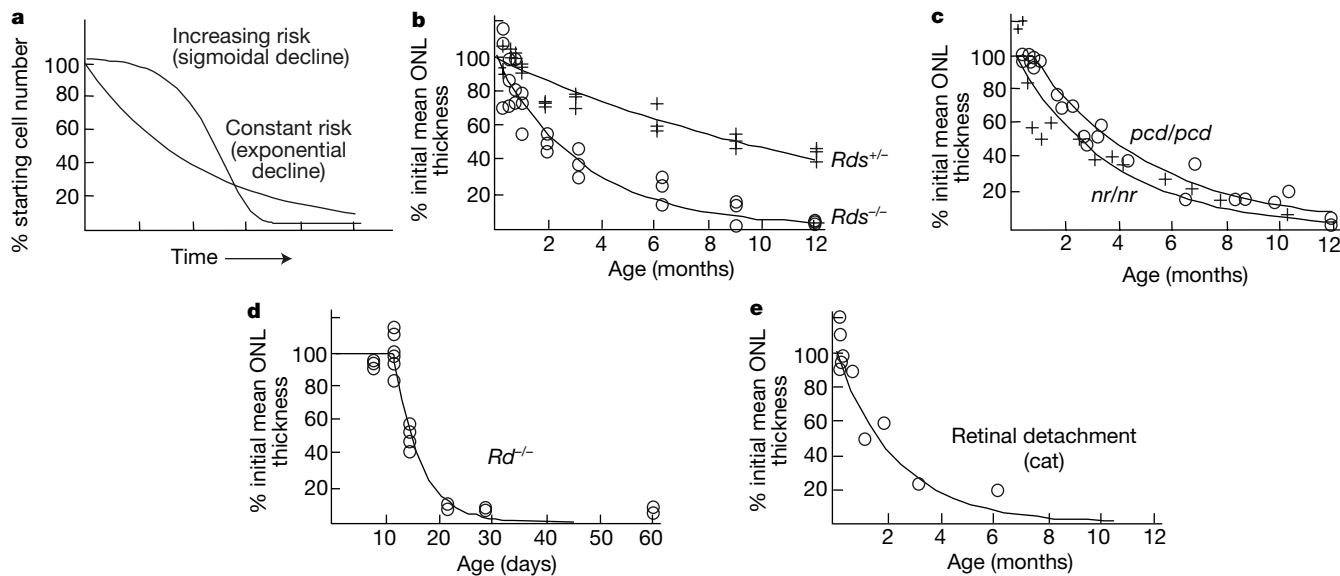
Figure 1 Animal models of inherited photoreceptor degeneration and retinal detachment, in which the kinetics of cell death are best described by a constant risk of neuronal death (see equations (1) and (3) in Methods). **a**, Constant and increasing risk of neuronal death will manifest as an exponential or sigmoidal decline in cell number, respectively. **b**, *Retinal degeneration slow* heterozygous ($Rds^{+/-}$)[15] and homozygous mice ($Rds^{-/-}$)[15] carrying a null mutation in the gene encoding peripherin/rds. **c**, *Nervous* homozygous mice (nr/nr)[27], and *purkinje cell degeneration* mice (pcd/pcd)[28]. **d**, Mice homozygous for a null mutation in the gene encoding the phototransduction enzyme rod cGMP β-phosphodiesterase ($Rd^{-/-}$)[14]. **e**, Experimental retinal detachment in the cat[24].

Table 1 Parameter estimates for kinetic models relating the risk of neuronal death (μ) to age

Animal model	Constant μ: $\frac{dONL(t)}{dt} = -\mu \times ONL(t)$			Exponentially decreasing μ: $\frac{dONL(t)}{dt} = -\mu_0 e^{-At} \times ONL(t)$			
	μ	ONL(0)	R^{2*}	μ_0	A	ONL(0)	R^{2*}
$Rds^{+/-}$ mice[15]	0.0170	49.4 μm	0.992	N/A	N/A	N/A	rejected†
$Rds^{-/-}$ mice[15]	0.0729	40.5 μm	0.968	N/A	N/A	N/A	rejected†
nr/nr mice‡[27]	0.278	50.1 μm	0.953	N/A	N/A	N/A	rejected†
Photoreceptors of pcd/pcd mice[28]	0.223	10.6 nuclei	0.992	N/A	N/A	N/A	rejected†
Retinal detachment (cat)‡[24]	0.00752	220 nuclei per mm	0.976	N/A	N/A	N/A	rejected†
$Rom1^{-/-}$ mice[13]	0.0316	37.7 μm	0.993	0.0666	0.103	41.9 μm	0.995
pd (miniature schnauzer)[12]	2.24	12.1 nuclei	0.979	3.13	1.12	13.1 nuclei	0.992
Albino (Balb/cHeA) mice[14]	0.00917	51.7 μm	0.995	0.0235	0.0485	51.7 μm	0.997
$rcd-1$ (Irish setter)[11,12]	0.0289	10.6 nuclei	0.957	0.0483	0.086	11.8 nuclei	0.970
$Rd^{-/-}$;$Rds^{-/-}$ mice[14]	0.123	45.4 μm	0.992	0.208	0.0912	45.3 μm	0.996
P23H rhodopsin-expressing transgenic rat§	0.0095	46.8 μm	0.975	0.0172	0.00752	55.0 μm	0.987
$Rd^{-/-}$ mice[14]	0.208	42.2 μm	0.985	N/A	N/A	N/A	rejected†
Cultured hippocampal neurons[8]	0.0773	100% of normal	0.996	N/A	N/A	N/A	rejected†
Parkinson's disease[10]	0.0858	100% of normal	0.919	N/A	N/A	N/A	rejected†
Granule cell degeneration in pcd/pcd mice[9]	0.006	5,999.52 cells	0.990	0.0076	0.0018	6,000 cells	0.990
Chemically-induced rat model of Parkinson's disease[19]‡	0.207	100% of normal	0.967	0.537	0.310	100%	0.999

*R^2 values reflect the proportion of data variability that is explained by the model. All reported R^2 values were statistically significant ($P < 0.001$).
† Parameter estimates were not significantly different from zero.
‡ Regressions performed on mean values reported in literature.
N/A, not applicable.
§ M. M. LaVail, personal communication.

chemically induced rat model of Parkinson's disease[19] (Fig. 3d) can both be described by either a constant or an exponentially decreasing risk of cell death (Table 1). We also measured ^{18}F-doxyglucose uptake in the caudate nuclei of patients with Huntington's disease as an indirect measure of neuronal loss. Because each of these patients was repeatedly tested at various times after clinical onset, the glucose uptake data, predictably, is highly variable in the whole population of patients (see Supplementary Information). Consequently, analysis of neuronal degeneration kinetics in this heterogeneous population necessitated the use of repeated-measures regression for each individual (see Methods). We found that neurodegeneration in these patients is also best described by a constant risk of cell death (Fig. 3e). Thus, our identification of similar cell death kinetics in five different types of neuron indicates that a constant or decreasing risk of cell death may be common to many forms of neurodegeneration. Although neuronal death is mediated by apoptosis in all photoreceptor degenerations examined (for example, refs 7, 20), it

remains to be determined whether a constant or exponentially decreasing risk of death will be found invariably to accompany neuronal apoptosis.

Although the available data do not allow us to distinguish conclusively between constant and exponentially decreasing risk, both models indicate that the time of death of an individual neuron is random. Nevertheless, the two models have quite different pathophysiological implications. In a process involving constant risk, the time of death of an individual neuron is not only random, but also independent of the time of death of any other neuron. In this case, the kinetics of neuronal degeneration are comparable to the simple exponential decay exhibited by radioactive compounds, and the different rates of photoreceptor degeneration (Fig. 1) are determined largely or solely by the mutant genotype. In contrast, exponentially decreasing risk indicates that the chance of cell death decreases in direct proportion to the number of remaining cells. Such kinetics could result from an increase in the concentration of a
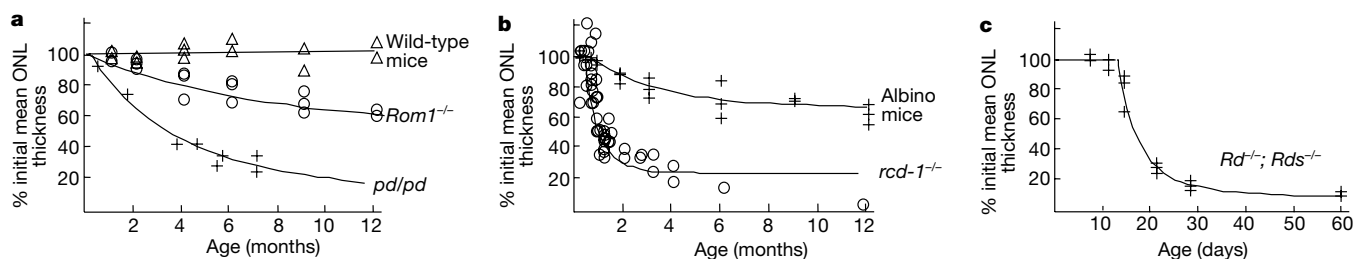
Figure 2 Animal models of inherited photoreceptor degeneration in which the kinetics of cell death are best described by an exponentially decreasing risk of death (see equations 1 and 2 in Methods). **a**, Wild-type and $Rom1^{-/-}$ mice[13], and photoreceptor dysplasia (pd/pd) in miniature schnauzers[12]. **b**, Albino mice[14] (Balb/cHeA) and rod-cell degeneration (rcd-1)

in Irish setters[11,12] due to a null mutation in the rod cGMP β-phosphodiesterase gene. **c**, Mice homozygous for null mutations in both the gene encoding rod cGMP β-phosphodiesterase and the gene encoding peripherin/rds ($Rd^{-/-}$;$Rds^{-/-}$)[14].
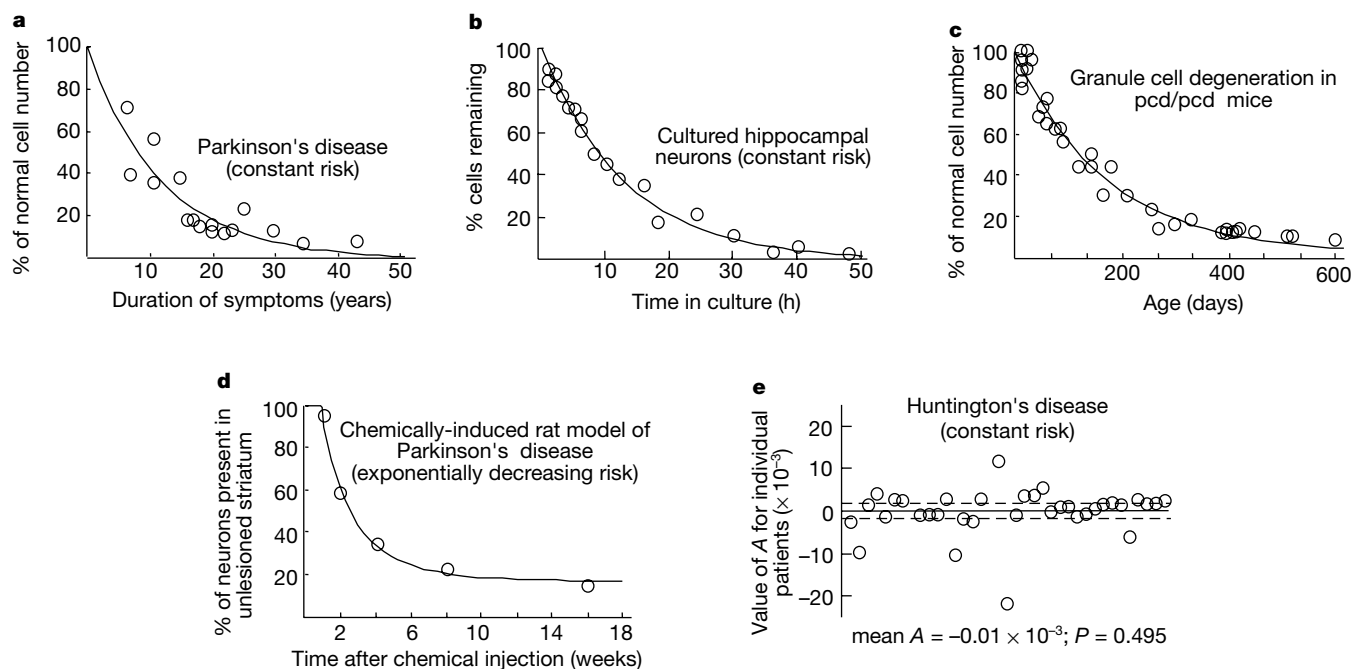
Figure 3 Examples of non-retinal neuronal death that display a constant or exponentially decreasing risk of death. **a**, The number of neurons (% of normal) in the substantia nigra of patients with Parkinson's disease as a function of symptom duration[10] is best described by a constant probability of neuronal death. **b**, Cultured hippocampal neurons undergoing excitotoxic cell death after incubation with glutamate exhibit a constant risk of cell death[8]. **c**, In contrast, the secondary loss of cerebellar granule cells[9] is described equally well by either a constant or an exponentially decreasing risk of cell death; the curve represents a constant risk. **d**, The percentage of substantia nigra neurons present in rats after injection

with the neurotoxin 6-hydroxydopamine[19], a chemically induced animal model of Parkinson's disease, is best fit by an exponentially decreasing risk of neuronal death. **e**, The kinetics of metabolic decline in Huntington's disease patients are best fit by a constant risk of cell loss. Values of A (in the exponent of equation (5), see Methods) do not differ significantly from zero ($P = 0.495$, Student's t-test). Each point represents the estimated A for an individual patient. Solid line, mean A (mean $\pm$ s.d.: $-0.01 \times 10^{-3} \pm 5.3 \times 10^{-3}$ mM h^{-1}, $n = 38$ patients) across patient population; dashed lines, 95% confidence interval for the mean value of A (-1.7×10^{-3}, 1.7×10^{-3}).

survival factor, such as basic fibroblast growth factor or ciliary neurotrophic factor[21], or from a decrease in the amount of a toxic factor as the population of cells declines. Consistent with the latter possibility, dying retinal progenitor cells have been shown to produce an apoptosis-inducing agent[22].

An alternative interpretation for the exponential decline in risk is that the decrease is an artefact resulting from the presence of two neuronal populations, each with different but constant risks of cell death. For photoreceptor degenerations, this possibility is excluded by the fact that 97% of mouse photoreceptors are rods and only 3% are cones[23]. This proportion of cones is too small to influence the overall kinetics of photoreceptor death. Furthermore, the data for all six models exhibiting a decreasing risk do not fit a simple equation incorporating two exponential functions (see Supplementary Information), which also suggests that the presence of two differentially affected cell populations is not responsible for the exponentially decreasing risk of cell death.
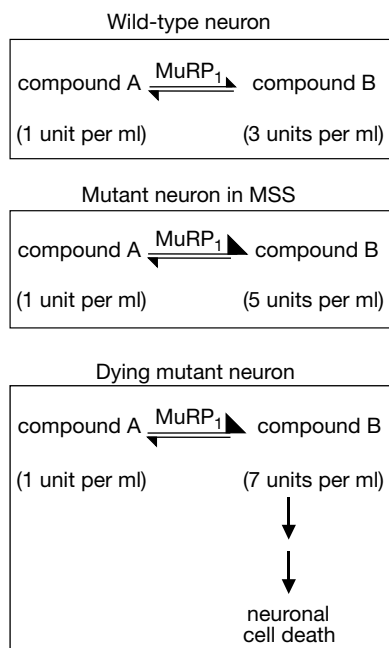
Any model of the mechanisms underlying inherited neuronal degenerations must account for the major features of cell death in these disorders. These features are (1) the constant or decreasing risk of neuronal death described above; (2) the genotype-dependent nature of the risk; (3) the random time of death of any cell (illustrated by the random distribution of apoptotic photoreceptors seen in the retinas of animals and humans with inherited retinal degenerations[13,20]); and (4) the paradoxical situation in which most neurons in animals or patients with inherited neurodegenerations survive and function normally for months, years or decades, while a few genetically identical cells in the population are dying randomly.

We propose that these features can be explained if the mutant neurons are in an abnormal homeostatic state, the mutant steady state (MSS). The MSS differs little from the normal neuronal steady state (as most of the mutant cells are alive and functioning normally), except that the MSS is associated with an increased risk of cell death. We suggest that the MSS is a response to mutation characterized by subtle but critical changes in the expression or function of relatively few 'mutant response' genes or proteins (MuRGs or MuRPs, respectively), which mediate critical pre-death reactions. If MuRP is an enzyme, for example, it may change the relative concentrations of 'pre-lethal' molecules (Fig. 4). Exit from the MSS and commitment to cell death would occur when random fluctuations in the concentrations of pre-lethal molecules exceed a threshold beyond which neuronal death is initiated. Different mutations would shift the steady state to varying degrees, so that mutations producing a transition to an MSS closer to the cell-death threshold have a greater chance of exceeding that threshold, and therefore a higher probability of causing cell death. Thus, we propose a 'one-hit' model in which the death of an individual neuron is initiated randomly in time by a single rare catastrophic event.

A similar one-hit kinetic model has been proposed and rejected as an explanation for the exponential cell death kinetics exhibited by cultured hippocampal neurons exposed transiently to excitotoxic amino acids[8]. The one-hit model was rejected in favour of a more complex mechanism involving a multistep biochemical cascade in which the overall death rate is determined by the specific rate constants for each of an unknown number of transitions within the cascade. We suggest, however, that some environmental insults place neurons in an abnormal steady state which, like the MSS, is associated with a constant increased risk of death. This environmentally induced abnormal steady state is exemplified by the effect of excitotoxic amino acids in initiating the exponential death of hippocampal neurons[8] (Fig. 3b, Table 1) and by the effect of retinal detachment in leading to photoreceptor death[24] (Fig. 1e, Table 1).

Our findings have important implications for the understanding and treatment of retinal and possibly other types of neuronal degeneration. First, biochemical mechanisms proposed to underlie neuronal death must be re-examined in light of the constant or exponentially decreasing risk of cell death that we have identified. Second, identification of the MuRGs and MuRPs in different mutant neurons will indicate whether mutations impose MSSs that share common MuRGs and MuRPs, or whether each MSS is uniquely or partly defined by the specific mutant gene or mutation. In mutant neurons in which the risk of death is constant throughout life, the MSS should be the same in young and old cells with the same genotype, although additional secondary changes in gene or protein expression may occur as a consequence of cell death. Alternatively, in models in which the risk of death decreases exponentially, cell death may be associated with a changing pattern of MuRGs and MuRPs. In either case, identification of MuRGs and MuRPs in different mutants is likely to provide insight into the pathogenic events that increase the risk of cell death in the MSS. Pharmacological intervention to shift the activity of MuRGs and MuRPs towards normal levels should slow or prevent initiation of the biochemical cascade leading to cell death. Finally, the absence of cumulative damage means that the likelihood that a mutant neuron can be rescued by treatment is not diminished by age, although fewer cells will be available to rescue. Therefore, treatment at any stage of the illness is likely to confer benefit. □

Wild-type neuron

compound A $\xrightarrow{\text{MuRP}_1}$ compound B

(1 unit per ml)   (3 units per ml)

Mutant neuron in MSS

compound A $\xrightarrow{\text{MuRP}_1}$ compound B

(1 unit per ml)   (5 units per ml)

Dying mutant neuron

compound A $\xrightarrow{\text{MuRP}_1}$ compound B

(1 unit per ml)   (7 units per ml)

↓

↓

neuronal cell death

Figure 4 The exponential kinetics of cell death in inherited neuronal degenerations suggest the existence of a mutant steady state (MSS) in which the risk of cell death is increased. In wild-type neurons, a reaction, catalysed for example by the enzyme MuRP$_1$, is associated with a concentration of compound B of 3 units per ml. In a mutant neuron in the MSS, the MuRP$_1$ activity changes in response to the mutation, so that the concentration of compound B is increased to 5 units per ml. Random increases in the concentration of compound B to 7 units per ml will trigger cell death.

Methods

Measurements and statistical analysis

We examined the kinetics of photoreceptor degeneration in animal models in which cell loss had been reported quantitatively over at least one year, or until most photoreceptors had died. The kinetics of cell loss were analysed by fitting either the outer nuclear layer (ONL) thickness or cell number data to solutions of the differential equation

$$\frac{d\text{ONL}(t)}{dt} = -\mu(t) \times \text{ONL}(t) \tag{1}$$

where $\mu(t)$ represents the risk of cell death at age t. Functions for $\mu(t)$ were substituted as

follows:

$$\text{exponentially decreasing risk} \quad \mu(t) = \mu_0 e^{-A(t-\text{delay})} \quad (2)$$

$$\text{constant risk} \quad \mu(t) = \mu_0 \quad (3)$$

$$\text{exponentially increasing risk} \quad \mu(t) = \mu_0 e^{A(t-\text{delay})} \quad (4)$$

where μ_0 represents the initial probability of cell death and delay represents the time before neuronal death begins. Equations for $\mu(t)$ were chosen on the basis of their ability to yield exponential and sigmoidal curves. Data fitting was performed using nonlinear regression analysis (quasi-Newton methods), a method of modelling the relationship between variables, using the functions in the Mathematica 3.0 (Wolfram Research) software package[25]. Models were rejected if parameter estimates did not differ significantly ($P < 0.05$) from zero.

Measurements of metabolic decline in the caudates of 38 patients with Huntington's disease were obtained from PET scans as described[26]. For each patient, average glucose uptake over the course of at least three years was fit to the solution of the differential equation:

$$\frac{d\text{ONL}(t)}{dt} = \mu e^{At} \times \text{ONL}(t) \quad (5)$$

to provide an estimate of A. $A > 0$ corresponds to increasing risk, $A < 0$ to decreasing risk, and $A = 0$ to constant risk. Estimates of A for each subject were then averaged, and a Student's t-test was used to determine whether the mean value was significantly different from zero ($P < 0.05$).

1. Coyle, J. T. & Puttfarken, P. Oxidative stress, glutamate, and neurodegenerative disorders. *Science* **262,** 689–695 (1993).
2. Cummings, J. L., Vinters, H. V., Cole, G. M. & Khachaturian, Z. S. Alzheimer's disease: etiologies, pathophysiology, cognitive reserve, and treatment opportunities. *Neurology* **51,** S2–17 (1998).
3. Alves-Rodrigues, A., Gregori, L. & Figueiredo-Pereira, M. E. Ubiquitin, cellular inclusions and their role in neurodegeneration. *Trends Neurosci.* **21,** 516–520 (1998).
4. Cassarino, D. S. & Bennett, J. P. Jr An evaluation of the role of mitochondria in neurodegenerative diseases: mitochondrial mutations and oxidative pathology, protective nuclear responses, and cell death in neurodegeneration. *Brain Res. Rev.* **29,** 1–25 (1999).
5. Selkoe, D. J. Translating cell biology into therapeutic advances in Alzheimer's disease. *Nature* **399,** A23–A31 (1999).
6. Dunnett, S. B. & Björklund, A. Prospects for new restorative and neuroprotective treatments in Parkinson's disease. *Nature* **399,** A32–A39 (1999).
7. Travis, G. H. Mechanisms of cell death in the inherited retinal degenerations. *Am. J. Hum. Genet.* **62,** 503–508 (1998).
8. Dubinsky, J. M., Kristal, B. S. & Elizondo-Fournier, M. On the probabilisitic nature of excitotoxic neuronal death in hippocampal neurons. *Neuropharmacology* **34,** 701–711 (1995).
9. Triarhou, L. C. Rate of neuronal fallout in a transsynaptic cerebellar model. *Brain Res. Bull.* **47,** 219–222 (1998).
10. Fearnley, J. M. & Lees, A. J. Ageing and Parkinson's disease: substantia nigra regional selectivity. *Brain* **114,** 2283–2301 (1991).
11. Schmidt, S. Y. & Aguirre, G. D. Reductions in taurine secondary to photoreceptor loss in Irish setters with rod-cone dysplasia. *Invest. Ophthalmol. Vis. Sci.* **26,** 679–683 (1985).
12. Parshall, C. J., Wyman, M., Nitroy, S., Acland, G. & Aguirre, G. Photoreceptor dysplasia: an inherited progressive retinal atrophy of miniature schnauzer dogs. *Prog. Vet. Comp. Ophthalmol.* **1,** 187–203 (1991).
13. Clarke, G. *et al.* Rom-1 is required for rod photoreceptor viability and the regulation of disk morphogenesis. *Nature Genet.* **25,** 67–73 (2000).
14. Sanyal, S. & Hawkins, R. K. Genetic interaction in the retinal degeneration of mice. *Exp. Eye Res.* **33,** 213–222 (1981).
15. Hawkins, R. K., Jansen, H. G. & Sanyal, S. Development and degeneration of retina in *rds* mutant mice: photoreceptor abnormalities in the heterozygotes. *Exp. Eye Res.* **41,** 701–720 (1985).
16. Massof, R. W., Dagnelie, G., Benzschawel, T., Palmer, R. W. & Finkelstein, D. First order dynamics of visual field loss in retinitis pigmentosa. *Clin. Vis. Sci.* **5,** 1–26 (1990).
17. Berson, E. L., Sandberg, M. A., Rosner, B., Birch, D. G. & Hanson, A. H. Natural course of retinitis pigmentosa over a three-year interval. *Am. J. Ophthalmol.* **99,** 240–251 (1985).
18. Birch, D. G., Anderson, J. L. & Fish, G. E. Yearly rates of rod and cone functional loss in retinitis pigmentosa and cone-rod dystrophy. *Ophthalmology* **106,** 258–268 (1999).
19. Sauer, H. & Oertel, W. H. Progressive degeneration of nigrostriatal dopamine neurons following intrastriatal terminal lesions with 6-hydroxydopamine: a combined retrograde tracing and immunocytochemical study in the rat. *Neuroscience* **59,** 401–415 (1994).
20. Li, Z.-Y. & Milam, A. H. in *Degenerative Diseases of the Retina* (eds Anderson, R. E., LaVail, M. M. & Hollyfield, J. G.) 1–8 (Plennum, New York, 1995).
21. Wen, R. *et al.* Injury-induced upregulation of bFGF and CNTF mRNAs in the rat retina. *J. Neurosci.* **15,** 7377–7385 (1995).
22. Seigal, G. S. & Liu, L. Inducible, apoptosis-promoting activity in retinal cell-conditioned medium. *Mol. Vision* **3,** 14 (1997).
23. Carter-Dawson, L. D. & LaVail, M. M. Rods and cones in the mouse retina. I. Structural analysis using light and electron microscopy. *J. Comp. Neurol.* **188,** 245–262 (1979).
24. Erickson, P. A., Fisher, S. K., Anderson, D. H., Stern, W. H. & Borgula, G. A. Retinal detachment in the cat: the outer nuclear and outer plexiform layers. *Invest. Ophthalmol. Vis. Sci.* **24,** 927–942 (1983).
25. Ratkowsky, D. A. *Nonlinear Regression Modeling: A Unified Practical Approach* (Marcel Decker, New York, 1983).
26. Kremer, B. *et al.* Influence of lamotrigine on progression of early Huntington's disease: a randomized clinical trial. *Neurology* **53,** 1000–1011 (1999).
27. La Vail, M. M. *et al.* Retinal degeneration in the nervous mouse. I. Light microscopic cytopathology and changes in the interphotoreceptor matrix *J. Comp. Neurol.* **333,** 168–181 (1993).
28. LaVail, M. M., Blanks, J. C. & Mullen, R. J. Retinal degeneration in the pcd cerebellar mouse. I. Light microscopic and autoradiographic analysis. *J. Comp. Neurol.* **212,** 217–230 (1982).

Genetic ablation of parathyroid glands reveals another source of parathyroid hormone

Thomas Günther*†, **Zhou-Feng Chen**†‡, **Jaesang Kim**§, **Matthias Priemel**‖, **Johannes M. Rueger**‖, **Michael Amling**‖, **Jane M. Moseley**¶, **T. John Martin**¶, **David J. Anderson**§ **& Gerard Karsenty***

* *Department of Molecular and Human Genetics, Program of Developmental Biology, Baylor College of Medicine, 1 Baylor Plaza, Houston, Texas 77030, USA*
‡ *Department of Anesthesiology, Washington University School of Medicine, 660 South Euclid Avenue, St. Louis, Missouri 63110, USA*
§ *Howard Hughes Medical Institute and Division of Biology, California Institute of Technology, Pasadena, California 91125, USA*
‖ *Department of Trauma Surgery, Hamburg University, Martinistrasse 52, 20246 Hamburg, Germany*
¶ *St. Vincent's Institute of Medical Research, 9 Princes Street, Fitzroy 3065, Melbourne, Victoria, Australia*
† *These authors contributed equally to this work*

The parathyroid glands are the only known source of circulating parathyroid hormone (PTH), which initiates an endocrine cascade that regulates serum calcium concentration[1]. *Glial cells missing2* (*Gcm2*), **a mouse homologue of** *Drosophila Gcm*, **is the only transcription factor whose expression is restricted to the parathyroid glands[2–5]. Here we show that** *Gcm2*-**deficient mice lack parathyroid glands and exhibit a biological hypoparathyroidism, identifying** *Gcm2* **as a master regulatory gene of parathyroid gland development. Unlike** *PTH receptor*-**deficient mice, however,** *Gcm2*-**deficient mice are viable and fertile, and have only a mildly abnormal bone phenotype. Despite their lack of parathyroid glands,** *Gcm2*-**deficient mice have PTH serum levels identical to those of wild-type mice, as do parathyroidectomized wild-type animals. Expression and ablation studies identified the thymus, where** *Gcm1,* **another Gcm homologue, is expressed, as the additional, downregulatable source of PTH. Thus,** *Gcm2* **deletion uncovers an auxiliary mechanism for the regulation of calcium homeostasis in the absence of parathyroid glands. We propose that this backup mechanism may be a general feature of endocrine regulation.**

Serum calcium is essential for many physiological functions including muscle contraction, blood coagulation, neuromuscular excitability and mineralization of bone, a tissue that contains 99%

Kainate receptors are involved in synaptic plasticity

Zuner A. Bortolotto*, Vernon R. J. Clarke*, Caroline M. Delany*,
Michael C. Parry*, Ilse Smolders*†, Michel Vignes*‡, Ken H. Ho§,
Peter Miu§, Bradford T. Brinton§, Robert Fantaske§, Ann Ogden‖,
Mary Gates‖, Paul L. Ornstein‖, David Lodge‖, David Bleakman‖
& Graham L. Collingridge*

* MRC Centre for Synaptic Plasticity, Department of Anatomy, Medical School,
University of Bristol, Bristol, BS8 1TD, UK
† Department of Pharmaceutical Chemistry & Drug Analysis, Pharmaceutical
Institute, Vrije Universiteit Brussels (VUB), Laarbeeklaan 103, 1090 Brussels,
Belgium
‡ Laboratoire 'Plasticité Cérébrale', EP 628 CNRS, Université Montpellier II, Place
Eugène Bataillon, 34095 Montpellier Cedex 05, France
§ Allelix Biopharmaceuticals, 6850 Goreway Drive, Mississauga, Ontario L4V 1V7,
Canada
‖ Eli Lilly & Co., Lilly Corporate Centre, Indianapolis 46285, Indiana, USA

The ability of synapses to modify their synaptic strength in response to activity is a fundamental property of the nervous system and may be an essential component of learning and memory[1]. There are three classes of ionotropic glutamate receptor, namely NMDA (*N*-methyl-D-aspartate), AMPA (α-amino-3-hydroxy-5-methyl-4-isoxazole-4-propionic acid) and kainate receptors[2]; critical roles in synaptic plasticity have been identified for two of these. Thus, at many synapses in the brain, transient activation of NMDA receptors leads to a persistent modification in the strength of synaptic transmission mediated by AMPA receptors[3,4]. Here, to determine whether kainate receptors[5–7] are involved in synaptic plasticity, we have used a new antagonist, LY382884 ((3S, 4aR, 6S, 8aR)-6-((4-carboxyphenyl)methyl-1,2,3,4,4a,5,6,7,8,8a-decahydroisoquinoline-3-carboxylic acid), which antagonizes kainate receptors at concentrations that do not affect AMPA or NMDA receptors. We find that LY382884 is a selective antagonist at neuronal kainate receptors containing the GluR5 subunit. It has no effect on long-term potentiation (LTP) that is dependent on NMDA receptors but prevents the induction of mossy fibre LTP, which is independent of NMDA receptors. Thus, kainate receptors can act as the induction trigger for long-term changes in synaptic transmission.

We have previously described two compounds, LY293558 ((3S, 4aR, 6R, 8aR)-6-[2-(1(2)H-tetrazol-5-yl)ethyl]-decahydroisoquinoline-3-carboxylic acid)[8] and LY294486 ((3SR, 4aRS, 6SR, 8aRS)-6-((((1H-tetrazol-5-yl) methyl) oxy) methyl)-1,2,3,4,4a,5,6,7,8,8a decahydroisoquinoline-3-carboxylic acid)[9], that inhibit responses mediated by kainate receptors containing the GluR5 but not the GluR6 subunit. However, these kainate receptor antagonists are also potent AMPA receptor antagonists, limiting their use except under circumstances where synaptic transmission mediated by AMPA receptors is blocked. We therefore examined other members of this family of decahydroisoquinoline compounds using ligand-binding assays; one compound, LY382884, was identified as
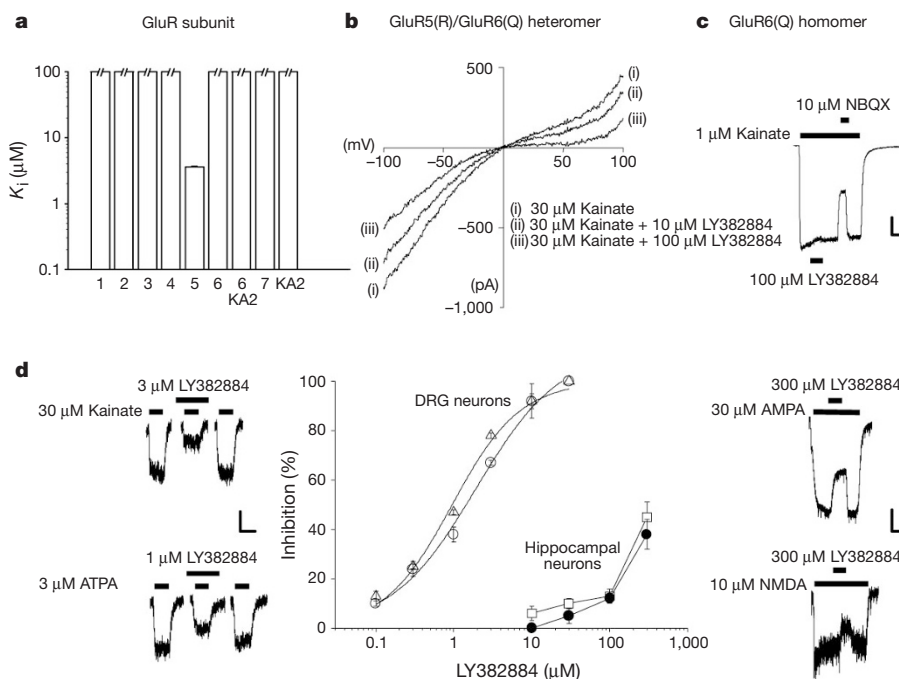

Figure 1 LY382884 is a selective GluR5 kainate receptor antagonist. **a**, Selective displacement of binding to human recombinant GluR5 receptors. K_i values were estimated from 11-point competition assays, from 3–4 separate preparations. Histograms with open tops indicate a binding affinity >100 μM (displacements using 100 μM LY382884: GluR1, 23 ± 5%; GluR2, 26 ± 3%; GluR3, 5 ± 3%; GluR4, 24 ± 2%; GluR6, 1 ± 1%; GluR7, 26 ± 6%; KA2, 8 ± 3%; GluR6 + KA2, 25 ± 16%). **b**, LY382884 antagonizes GluR5/GluR6 heteromeric receptors. A voltage ramp was applied during steady-state responses to kainate (30 μM). Cells with a significant response generated by heteromeric receptors were characterized by less rectification than homomeric GluR6(Q) (the ratio of currents at +50/−50 mV was 0.66 ± 0.07 for heteromeric receptors ($n = 8$) and 0.06 ± 0.03 for homomeric GluR6(Q) ($n = 5$). Kainate currents were inhibited by LY382884 (10 and 100 μM) by 18 ± 3 and 41 ± 3%, respectively (−50 mV), and by 30 ± 6 and 70 ±

6%, respectively (+50 mV). The voltage-dependence of the antagonism was significant ($P < 0.01$, $n = 8$). **c**, LY382884 does not affect 1 μM kainate currents in cells expressing homomeric GluR6(Q) (4 ± 3%; $n = 3$). The effectiveness of NBQX (10 μM) is shown for comparison. Holding voltage (V_h) = −70 mV; scale bar represents 100 pA vertical and 10 s horizontal. (LY382884 (100 μM) also had little effect on 30 μM kainate currents in GluR6(Q) homomers (6 ± 1%; $n = 5$)). **d**, Functional selectivity of LY382884 at native ionotropic glutamate receptors. The graph shows concentration-dependent antagonism by LY382884 of responses of DRG neurons to 3 μM ATPA (triangles) and 30 μM kainate (open circles) and of hippocampal neurons to 10 μM NMDA (filled circles) and 30 μM AMPA (squares) (V_h = −70 mV). Data were obtained from at least three separate cells at each concentration. Scale bars for representative currents are 50 pA (kainate), 75 pA (ATPA), 200 pA (AMPA) and 50 pA (NMDA) (vertical) and 10s (horizontal).

having considerably greater selectivity for GluR5 than for GluR2 (ref. 10). The ability of LY382884 to displace binding at a wide range of recombinant AMPA and kainate receptors is shown in Fig. 1a. Binding to GluR5 was displaced with an inhibition constant (K_i) of $4.0 \pm 0.2\ \mu M$ ($n = 4$), whereas binding to GluR1–4, GluR6, GluR7, KA2 and a heteromeric assembly of GluR6 and KA2 was displaced with K_i values in excess of $100\ \mu M$. The kainate receptor antagonist activity of LY382884 is shown for recombinant and native receptors in Fig. 1b–d. LY382884 antagonized kainate-induced currents in GluR5/GluR6 heteromers (Fig. 1b) but not in GluR6 homomers (Fig. 1c). The heteromer was made by co-expressing GluR6(Q), which alone generated strongly rectifying currents, with GluR5(R), which alone was non-functional; this co-expression yielded a more linear $I-V$ relationship than GluR6 alone, in response to voltage ramps between -100 and $+100\ mV$. In cells displaying this more linear rectification, LY382884 dose dependently reduced the current induced by $30\ \mu M$ kainate and increased rectification, presumably because a greater proportion of GluR6 homomers contributed to the residual current (Fig. 1b). The absence of functional antagonism at recombinant GluR6 kainate receptors is shown in Fig. 1c, which compares LY382884 with the AMPA/ kainate receptor antagonist NBQX (2,3-dihydroxy-6-nitro-7-sulphamoylbenzo(f)quinoxaline). LY382884 had no observable antagonistic effects at human GluR6 kainate receptors at concentrations of up to $100\ \mu M$. In rat dorsal root ganglion (DRG) neurons, which express GluR5 kainate receptors[8,11,12], LY382884 inhibited currents evoked by kainate ($30\ \mu M$) and a selective GluR5 kainate receptor ligand, ATPA ((RS)-2-amino-3-(3-hydroxy-5-$tert$-butylisoxazol-4-yl)propanoic acid) ($3\ \mu M$) in a concentration-dependent manner (half maximal concentration (IC_{50}) $0.95 \pm 0.16\ \mu M$ ($n = 6$) and $1.19 \pm 0.79\ \mu M$ ($n = 6$), respectively). We also established the antagonistic activity of LY382884 at hippocampal AMPA and NMDA receptors (Fig. 1d). LY382884 had little or no effect on currents evoked by AMPA ($30\ \mu M$) or NMDA ($10\ \mu M$) at a concentration of $10\ \mu M$.

To determine whether LY382884 can be used to antagonize neuronal kainate receptors selectively in an intact slice preparation, we performed experiments on the CA1 region of the hippocampus. We recorded excitatory postsynaptic potentials (EPSPs) mediated by AMPA receptors intracellularly and determined their sensitivity by sequentially applying increasing concentrations of the antagonist. LY382884 depressed the synaptic AMPA receptor-mediated response with an IC_{50} of $87\ \mu M$ ($n = 3$; Fig. 2a). In these experiments, $10\ \mu M$ was the maximum concentration that could be used before AMPA receptor-mediated synaptic transmission was affected. Neither monosynaptic γ-aminobutyric acid (GABA)$_A$ and GABA$_B$ receptor-mediated synaptic transmission[13] nor passive membrane properties were affected by $10\ \mu M$ LY382884 ($n = 5$; data not shown). Next, we determined the effectiveness of $10\ \mu M$ LY382884 as a kainate receptor antagonist by testing its ability to inhibit the depression of AMPA receptor-mediated synaptic transmission induced by ATPA, using field potential recordings in slices obtained from juvenile rats[14]. ATPA depressed field EPSPs (fEPSPs), at a concentration of $1\ \mu M$ ($n = 5$) or $3\ \mu M$ ($n = 6$), respectively, by 57 ± 6 and $63 \pm 6\%$ under control conditions but by only 6 ± 2 and $18 \pm 9\%$ in the presence of LY382884 (data not shown).

Given the high density of kainate receptors in area CA3 (ref. 15), we extended our analysis to this region. LY382884 similarly antagonized the depression of AMPA receptor-mediated EPSPs induced by ATPA. Thus, $1\ \mu M$ ATPA depressed associational/commissural and mossy-fibre-evoked fEPSPs, respectively, by 34 ± 2 and $42 \pm 11\%$ under control conditions but by only 6 ± 4 and $10 \pm 5\%$ in the presence of $10\ \mu M$ LY382884 ($n = 4$; Fig. 2b). Synaptic transmission in area CA3 is also inhibited by activation of metabotropic glutamate (mGlu) receptors, raising the possibility that ATPA and LY382884 are acting through these receptors. However, the mGlu receptor antagonist (S)-α-methyl-4-carboxyphenylglycine (MCPG) had no effect on ATPA-induced depression ($n = 5$), and LY382884
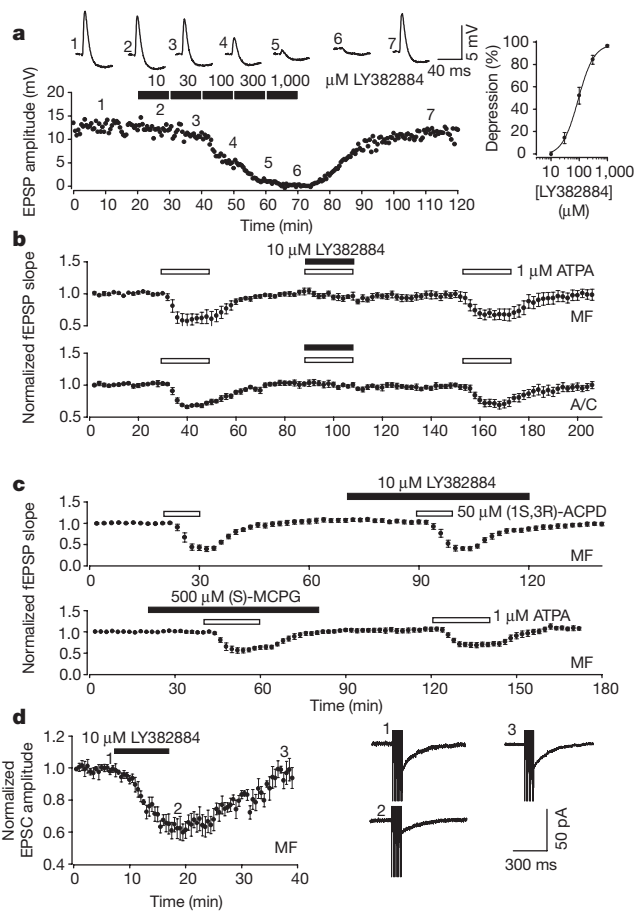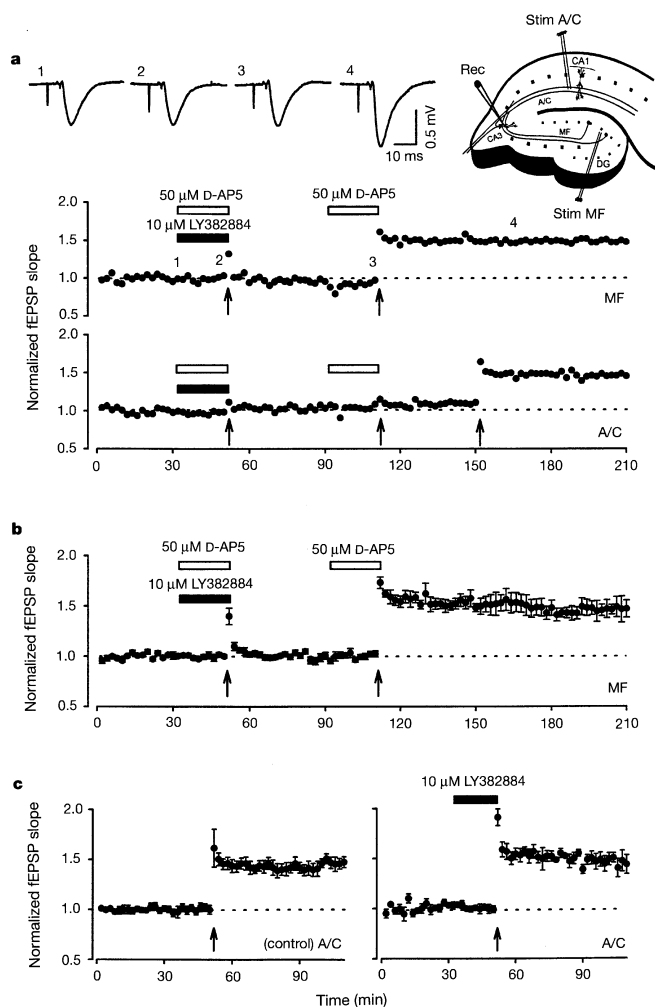

Figure 2 LY382884 as an antagonist in rat hippocampal slices. **a**, Concentration-dependent antagonism of AMPA receptor-mediated EPSPs. The left graph shows a single representative example and the right graph plots peak synaptic depression versus [LY382884] for three neurons ($EC_{50} = 87\ \mu M$; neurons held at $-73 \pm 3\ mV$). **b**, Pooled data ($n = 4$) showing reversible antagonism by LY382884 of ATPA-induced depression of field EPSPs in area CA3, evoked alternatively by stimulation of mossy fibres (MF) and associational/commissural (A/C) inputs. **c**, Pooled data to show that LY382884 does not affect (1S,3R)-ACPD-induced depression ($n = 6$) and that MCPG does not affect ATPA-induced depression ($n = 5$) of mossy-fibre-evoked fEPSPs. **d**, Reversible antagonism by LY382884 of kainate receptor-mediated EPSCs, evoked by high-frequency stimulation (10 shocks at 100 Hz) of mossy fibres, in the presence of a cocktail of antagonists[16] to prevent activation of AMPA, NMDA or GABA receptor-mediated synaptic currents ($n = 7$).

had no effect on depression induced by the mGlu receptor agonist (1S,3R)-1-aminocyclopentane-1,3-dicarboxylic acid ((1S,3R)-ACPD; $n = 6$; Fig. 2c). Furthermore, $10\ \mu M$ LY382884 had no effect on depolarization of CA3 neurons induced by $30\ \mu M$ (RS)-DHPG ((RS)-3,5-dihydroxyphenylglycine) (mean depolarizations before and after addition of LY382884, 10 ± 3 and $12 \pm 2\ mV$, respectively; $n = 8$), precluding an effect of the antagonist on postsynaptic group I mGlu receptors. CA3 neurons possess postsynaptic kainate receptors that can be activated synaptically by brief, high frequency tetanus[16,17]. LY382884 ($10\ \mu M$) antagonized this kainate receptor-mediated excitatory postsynaptic current (EPSC), recorded under whole-cell voltage-clamp conditions at $-70\ mV$, by $38 \pm 4\%$ ($n = 7$; Fig. 2d).

Having established that LY382884 is a selective kainate receptor antagonist, we wished to determine whether kainate receptors are involved in the induction of LTP at mossy fibre synapses, given that
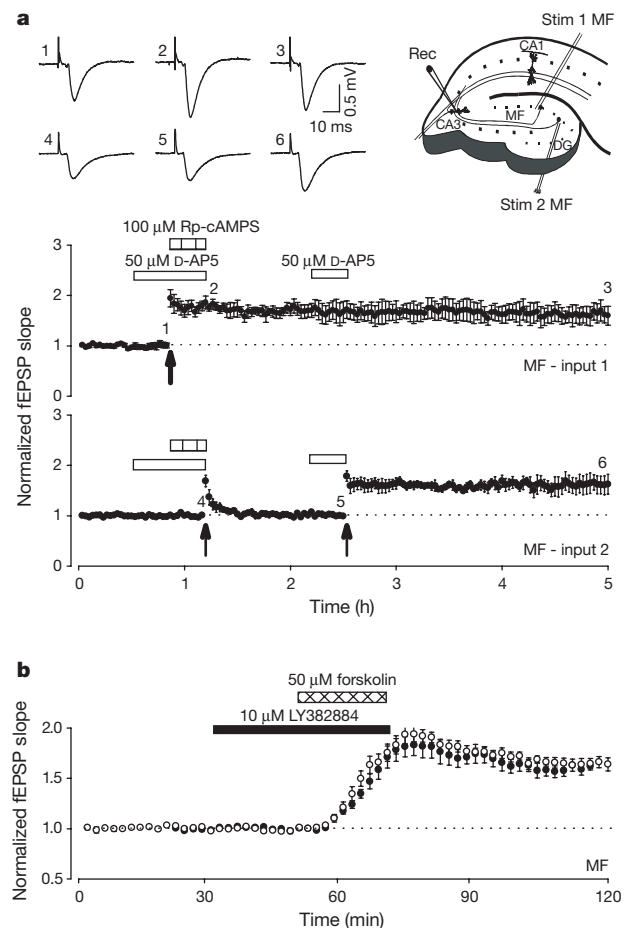
LTP at these synapses is classically independent of NMDA receptors[18]. Mossy fibre LTP was completely prevented, in a reversible manner, by LY382884. (The mean potentiation 60 min after tetanization (100 Hz, 1 s, test intensity) in the presence and after washout of LY382884 was 1 ± 4% and 48 ± 10%, respectively; $n = 7$; Fig. 3a, b.) The ability of LY382884 to block the induction of LTP was pathway specific, as NMDA receptor-dependent LTP in the CA3 region of the hippocampus, evoked by tetanic stimulation of associational/commissural fibres, was fully resistant to the actions of LY382884. The mean potentiation 60 min after tetanization in the presence of LY382884 was 45 ± 10 ($n = 3$), compared with 47 ± 6% in interleaved control experiments ($n = 6$; Fig. 3c). Furthermore, NMDA receptor-dependent LTP at CA1 synapses was also insensitive to LY382884 ($n = 7$; data not shown).

It was possible that LY382884 blocked the induction of LTP by an action that was independent of its ability to antagonize kainate receptors. Mossy fibre LTP involves the activation of the cAMP–protein kinase A (PKA) pathway and can be induced by the stimulation of adenylyl cyclase by forskolin[19]. Figure 4a shows input-specific, long-lasting (>4 h), PKA-dependent mossy fibre LTP induced by our standard tetanus protocol. LY382884 had no effect on forskolin-induced mossy fibre LTP ($n = 6$) when compared with interleaved controls ($n = 6$; Fig. 4b). Thus, its ability to inhibit LTP is unlikely to be due to an action on signal transduction or expression mechanisms involved in mossy fibre LTP.

The finding that kainate receptors are involved in the induction of mossy fibre LTP is unexpected, as two other antagonists, kynurenate and CNQX, have been reported not to block mossy-fibre-induced LTP[20,21]. We confirmed that kynurenate could cause substantial antagonism of AMPA receptor-mediated synaptic transmission without preventing the induction of LTP, as determined following washout of kynurenate (this result was observed when 3 mM was applied for 20 min, our standard perfusion time to achieve a steady-state concentration; Fig. 5a). We verified that AMPA receptors are not required for induction of mossy fibre LTP using GYKI53655 (30 μM, 20 min), a more selective AMPA receptor antagonist, which

Figure 3 LY382884 specifically blocks the induction of mossy fibre LTP. **a**, A single example to show reversible block of the induction of mossy fibre (MF) LTP by LY382884. Note that the tetani were delivered in the presence of the NMDA receptor antagonist D-AP5, except for the third tetanus delivered to the associational/commissural (A/C) fibres. The traces in this and subsequent figures are averages of four successive records obtained at the times indicated on the graphs by the corresponding numbers. Inset, positions of the stimulating and recording electrodes. **b**, Pooled data for seven experiments showing reversible block of mossy-fibre-induced LTP. In this and subsequent graphs, data points are the average of four successive measurements and the time of each tetanus (100 Hz, 1 s, test intensity) is indicated by an arrow. **c**, The pooled data shows NMDA receptor-dependent LTP in the CA3 region of the hippocampus, evoked by tetanic stimulation of A/C fibres, under control conditions ($n = 6$) and in the presence of LY382884 ($n = 3$).

Figure 4 LY382884 does not affect forskolin-induced LTP. **a**, Pooled data ($n = 3$) to show that a single tetanus, delivered in the presence of D-AP5, induced input-specific, PKA-dependent LTP that lasted at least 4 h. Note that Rp-cAMPS (Rp-adenosine 3,5-cyclic monophosphothioate triethylamine) was applied immediately after tetanization of input 1 and washout was commenced immediately after tetanization of input 2. Inset, electrode arrangements. **b**, Pooled data to show that LY382884 does not affect LTP induced by application of forskolin. Data are from six slices treated with LY382884 (open symbols) and six interleaved controls (filled circles). Forskolin produced no potentiation of the associational/commissural input (data not shown).

reversibly blocked mossy fibre synaptic transmission. Three hours after the start of washout of GYKI53655, the non-tetanized input had recovered to baseline values (+5 ± 2%), whereas the tetanized input exhibited stable LTP (of 89 ± 25%; $P < 0.05$; $n = 5$).

LTP was, however, fully blocked by 10 mM kynurenate ($n = 5$; Fig. 5b). We also found that 10 μM CNQX, a concentration that antagonizes kainate-induced currents mediated by GluR5 in CA3 neurons[16], blocked the induction of mossy fibre LTP ($n = 4$; Fig. 5c). In these two sets of experiments, we also examined the effects of LY382884 alone and of D(-)-2-amino-5-phosphonopentanoate (D-AP5) alone on mossy fibre LTP; in all cases, LY382884 blocked LTP whereas LTP was readily obtained in the presence of D-AP5 (the mean potentiation 60 min after tetanization in the presence of LY382884 alone was −2 ± 1%; 60 min after tetanization in the presence of D-AP5 alone it was 36 ± 11%; $n = 9$). CNQX (K_i for displacement of GluR5 binding, 2.9 ± 0.2 μM; $n = 3$) is about as effective as LY382884, whereas kynurenate is very weak as an antagonist at GluR5-expressing cells, with dose-dependent antagonism over the millimolar range. In three separate systems, kynurenate produced significantly ($P < 0.05$) more antagonism at 10 mM than at 3 mM: displacement of 100-μM kainate binding in GluR5-expressing HEK293 cells was 98 ± 1% at 10 mM kynurenate and 60 ± 1% at 3 mM ($n = 3$); inhibition of 100 μM kainate currents in DRG neurones was 89 ± 3 and 76 ± 1%, respectively ($n = 3$); depression of synaptic responses mediated by kainate receptors in CA3 neurons was 84 ± 7 and 42 ± 8%, respectively ($n = 4$). Thus, three structurally unrelated compounds antagonized both events mediated by kainate receptors containing GluR5 and mossy fibre LTP in the same rank order of potency: LY382884 = CNQX ≫ kynurenate.

LY382884 shows selectivity between homomeric GluR5 and GluR2 receptors[10]; it has been used in studies of global ischaemia[10] and nociception[22,23]. We have shown that LY382884 antagonizes responses mediated by kainate receptors at concentrations below those that affect synaptic processes mediated by AMPA or NMDA receptors. Like LY293558 (ref. 8) and LY294486 (ref. 9), LY382884 is highly selective for the GluR5 kainate receptor subunit. The earlier kainate receptor antagonists have been used to identify a role for GluR5 subunits in excitatory synaptic transmission in the hippocampus[24,25] and amygdala[26]. However, these compounds also antagonize AMPA receptors. Given its greater selectivity, LY382884 is a more useful antagonist with which to explore the functions of GluR5 in the brain.

Although our data indicate that the kainate receptor involved in the induction of LTP may have at least one GluR5 subunit, this does not preclude roles for other kainate receptor subunits in synaptic plasticity. Indeed, as the kainate receptor-mediated component of excitatory synaptic transmission at mossy fibre synapses[16,17] is both antagonized by GluR5 antagonists[24] and absent in GluR6 knockout mice[27], both subunits may contribute to native kainate receptors in these neurons. The sensitivity of a GluR5/GluR6 heteromer to LY382884 is consistent with this possibility. Our findings do not indicate whether mossy fibre LTP is induced pre- or postsynaptically[28,29], as GluR5-containing kainate receptors are located at both sites. However, it may be possible to develop antagonists that are selective for pre- or postsynaptic kainate receptors at mossy fibres to address this question. Other receptors, such as mGlu receptors, may activate separate transduction processes that are also required for mossy fibre LTP[20,29,30]. Hitherto, LTP has been viewed as usually being induced by the synaptic activation of NMDA receptors and expressed as an enhancement of synaptic transmission mediated by AMPA, and under certain circumstances NMDA, receptors[3]. At synapses that exhibit LTP independently of NMDA receptors, it has been assumed that ionotropic glutamate receptors are not required for the induction of LTP[28,29]. We have shown that kainate receptors are involved in the induction of LTP at a synapse where NMDA receptors do not have a role. It will be
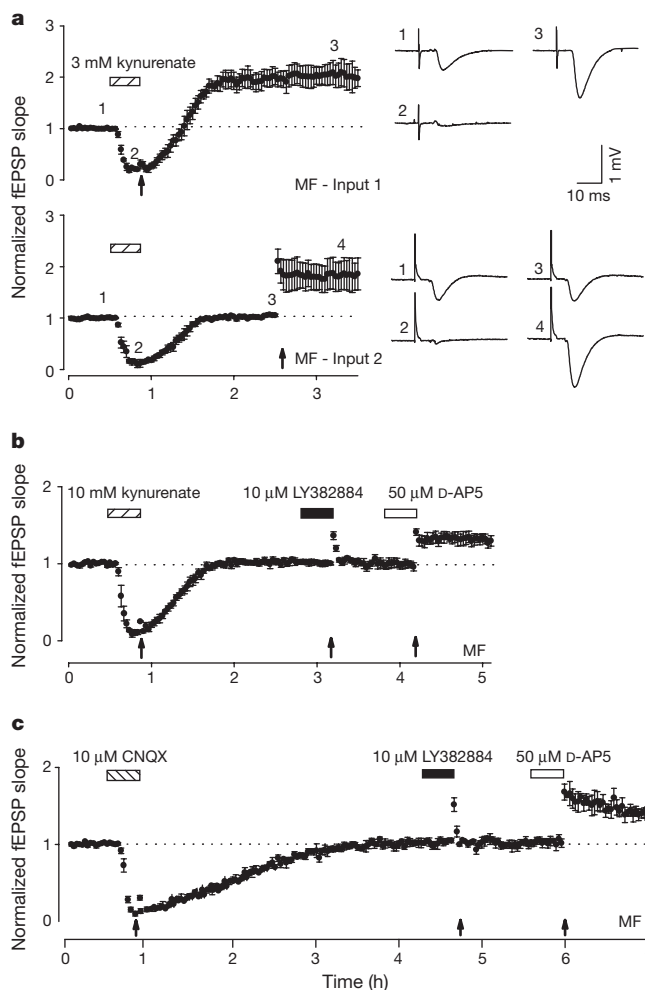
Figure 5 Kynurenate and CNQX block the induction of mossy fibre LTP. **a**, Pooled data ($n = 4$) to show that 3 mM kynurenate blocks AMPA receptor-mediated synaptic transmission but not mossy fibre LTP. A tetanus was delivered to input 1 during blockade of synaptic transmission and to input 2 following recovery from the effects of kynurenate. The traces are from a single experiment. **b**, Pooled data ($n = 5$) to show that 10 mM kynurenate, like 10 μM LY382884, blocks the induction of mossy fibre LTP. **c**, Pooled data ($n = 4$) to show that 10 μM CNQX, like 10 μM LY382884, blocks the induction of mossy fibre LTP.

interesting to determine whether this principle extends to other synapses where NMDA receptor-independent LTP has been found and whether, by analogy to the NMDA receptor, the biophysical properties of kainate receptors[5–7] endow properties of functional significance to this form of LTP.

Methods

Ligand-binding studies

These experiments were performed using cell membranes prepared from frozen HEK293 cells expressing recombinant AMPA or kainate receptor subunits and using [3H]-AMPA and [3H]-kainate, respectively, as described[9].

Construction of the heteromer

A GluR6(Q) stable HEK293 cell line was transfected with GluR5$_{2b}$(R) in the vector pCEP4, using Lipofectamine 2000. After three weeks of selection with 250 μg ml⁻¹ hygromycin, the cells reached 30% confluency and were split for electrophysiology.

Electrophysiology using isolated cells

Whole-cell voltage clamp recordings were made using extracellular solutions comprising (in mM) NaCl (138), CaCl$_2$ (5), KCl (5), MgCl$_2$ (1), HEPES (10) and glucose (10); pH 7.4.

For HEK293 cells and hippocampal neurons, intracellular solutions comprised (in mM) CsCl (140), $MgCl_2$ (1), diTris creatine phosphate (14), HEPES (10), BAPTA (15) and creatine phosphokinase (50 units ml^{-1}); pH 7.15. For DRG neurons[8], intracellular solutions comprised (in mM) $CsMeSO_4$ (125), CsCl (15), CsBAPTA (5), HEPES (10), $CaCl_2$ (0.5) $MgCl_2$ (3) and MgATP (2); pH 7.2. Experiments were performed at room temperature (20–22 °C). Drugs were applied by bath perfusion and exchange of solutions under these conditions took about 5 s. Voltage ramps were conducted between −100 and +100mV in 1 s. Experiments using recombinant receptors and DRG neurons were performed after incubation of cells with 250 μg ml^{-1} concanavalin A for 10 min to remove receptor desensitization. Hippocampal pyramidal neurons were cultured from E17 Sprague Dawley rat fetuses. AMPA receptor-mediated currents were obtained from cells (6–12 days *in vitro*) in the presence of tetrodotoxin (1 μM); NMDA receptor-mediated currents were recorded from cells (10–12 days *in vitro*) in the presence of glycine (10 μM) but without added magnesium. Curve fitting to the data points was based upon the equation $y = 100(D^n/(D^n + EC_{50}^n))$ using a slope fixed to a value of 1 and where D is the drug concentration. For antagonists, $EC_{50} = IC_{50}$. IC_{50} values were estimated from data obtained from at least four separate cells.

Electrophysiology in slice

Experiments were performed on transverse rat hippocampal slices (400 μm) maintained in medium comprising (in mM) NaCl (124), KCl (3), $NaHCO_3$ (26), NaH_2PO_4 (1.25), $CaCl_2$ (2), $MgSO_4$ (1) and D-glucose (10) (bubbled with O_2/CO_2 : 95/5%). Extracellular fEPSPs were recorded in areas CA1 and CA3 using glass microelectrodes (2–4 MΩ) containing 4 M NaCl, as described[14]. Intracellular recordings were obtained using sharp glass microelectrodes (40–80 MΩ) filled with $KMeSO_4$ (2M)[13]. Whole-cell patch-clamp recordings were obtained blind using glass microelectrodes (5–7 MΩ; seal resistance ∼10 GΩ) filled with a solution comprising (in mM) $CsMeSO_3$ (120), NaCl (1), $MgCl_2$ (1), Mg-ATP (4), BAPTA (10), N-(2,6-dimethyl-phenylcarbamoylmethyl)-triethylammonium bromide (QX-314) (5) and HEPES (5), adjusted to pH 7.3, as described[16]. Data are presented as mean ± s.e.m. throughout.

1. Hebb, D. O. *The Organization of Behaviour* (John Wiley, New York, 1949).
2. Watkins, J. C. & Evans, R. H. Excitatory amino acid transmitters. *Annu. Rev. Pharmacol. Toxicol.* **21**, 165–204 (1981).
3. Bliss, T. V. P. & Collingridge, G. L. A synaptic model of memory: Long-term potentiation in the hippocampus. *Nature* **361**, 31–39 (1993).
4. Bear, M. F. & Abraham, W. C. Long-term depression in hippocampus. *Annu. Rev. Neurosci.* **19**, 437–462 (1996).
5. Bettler, B. & Mulle, C. AMPA and kainate receptors. *Neuropharmacology* **34**, 123–139 (1995).
6. Bleakman, D. & Lodge, D. Neuropharmacology of AMPA and kainate receptors. *Neuropharmacology* **37**, 1187–1204 (1998).
7. Chittajallu, R., Braithwaite S. P., Clarke, V. R. J. & Henley, J. M. Kainate receptors: subunits, synaptic localization and function. *Trends Pharmacol. Sci.* **20**, 26–35 (1999).
8. Bleakman, D. *et al.* Pharmacological discrimination of GluR5 and GluR6 kainate receptor subtypes by (3S,4aR,6R,8aR)-6-[2-(1(2)H- tetrazole-5-yl)ethyl]decahydroisoquinoline-3 carboxylic acid. *Mol. Pharmacol.* **49**, 581–585 (1996).
9. Clarke, V. R. J. *et al.* A hippocampal GluR5 kainate receptor regulating inhibitory synaptic transmission. *Nature* **389**, 599–603 (1997).
10. O'Neill, M. J. *et al.* Decahydroisoquinolines: novel competitive AMPA/kainate antagonists with neuroprotective effects in global cerebral ischaemia. *Neuropharmacology* **37**, 1211–1222 (1998).
11. Huettner, J. E. Glutamate receptor channels in rat DRG neurons: Activation by kainate and quisqualate and blockade of desensitization by Con A. *Neuron* **5**, 255–266 (1990).
12. Partin, K. M. *et al.* Selective modulation of desensitization at AMPA versus kainate receptors by cyclothiazide and concanavalin A. *Neuron* **11**, 1069–1082 (1993).
13. Davies, S. N. & Collingridge, G. L. Role of excitatory amino acid receptors in synaptic transmission in area CA1 of rat hippocampus. *Proc. R. Soc. Lond. B* **236**, 373–384 (1989).
14. Vignes, M. *et al.* The GluR5 subtype of kainate receptor regulates excitatory synaptic transmission in areas CA1 and CA3 of the rat hippocampus. *Neuropharmacology* **37**, 1269–1277 (1998).
15. Monaghan, D. T. & Cotman, C. W. The distribution of [^{3}H]kainic acid binding sites in rat CNS as determined by autoradiography. *Brain Res.* **252**, 91–100 (1982).
16. Vignes, M. & Collingridge, G. L. The synaptic activation of kainate receptors. *Nature* **388**, 179–182 (1997).
17. Castillo, P. E., Malenka, R. C. & Nicoll, R. A. Kainate receptors mediate a slow postsynaptic current in hippocampal CA3 neurons. *Nature* **388**, 182–186 (1997).
18. Harris, E. W. & Cotman, C. W. Long-term potentiation of guinea pig mossy fiber responses is not blocked by N-methyl-D-aspartate antagonists. *Neurosci. Lett.* **70**, 132–137 (1986).
19. Weisskopf, M. G., Castillo, P. E., Zalutsky, R. A. & Nicoll, R. A. Mediation of hippocampal mossy fiber long-term potentiation by cyclic AMP. *Science* **265**, 1878–1882.
20. Ito, I. & Sugiyama, H. Roles of glutamate receptors in long-term potentiation at hippocampal mossy fiber synapses. *NeuroReport* **2**, 333–336 (1991).
21. Castillo, P. E., Weisskopf, M. G. & Nicoll, R. A. The role of Ca^{2+} channels in hippocampal mossy fiber synaptic transmission and long-term potentiation. *Neuron* **12**, 261–269 (1994).
22. Simmons, R. M. A. *et al.* Kainate GluR5 receptor subtype mediates the nociceptive response to formalin in the rat. *Neuropharmacology* **37**, 25–36 (1998).
23. Procter, M. J. *et al.* Actions of kainate and AMPA selective glutamate receptor ligands on nociceptive processing in the spinal cord. *Neuropharmacology* **37**, 1287–1297 (1998).
24. Vignes, M., Bleakman, D., Lodge, D. & Collingridge, G. L. The synaptic activation of the GluR5 subtype of kainate receptor in area CA3 of the rat hippocampus. *Neuropharmacology* **36**, 1477–1481 (1997).
25. Cossart, R. *et al.* GluR5 kainate receptor activation in interneurons increases tonic inhibition of pyramidal cells. *Nature Neurosci.* **1**, 470–478 (1998).
26. Li, H. & Rogawski, M. A. GluR5 kainate receptor mediated synaptic transmission in rat basolateral amygdala *in vitro*. *Neuropharmacology* **37**, 1279–1286 (1998).
27. Mulle, C. *et al.* Altered synaptic physiology and reduced susceptibility to kainate-induced seizures in GluR6-deficient mice. *Nature* **392**, 601–605 (1998).
28. Nicoll, R. A. & Malenka, R. C. Contrasting properties of two forms of long-term potentiation in the hippocampus. *Nature* **377**, 115–118 (1995).
29. Yeckel, M. F., Kapur, A. & Johnston, D. Multiple forms of LTP in hippocampal CA3 neurons use a common postsynaptic mechanism. *Nature Neurosci.* **2**, 625–633 (1999).
30. Bashir, Z. I. *et al.* Induction of LTP in the hippocampus needs synaptic activation of glutamate metabotropic receptors. *Nature* **363**, 347–350 (1993).

....

Activation of the epithelial Na+ channel (ENaC) requires CFTR Cl− channel function

M. M. Reddy, M. J. Light & P. M. Quinton

Department of Pediatrics-0831, University of California, San Diego, School of Medicine, La Jolla, California 92093-0831, USA

....

It is increasingly being recognized that cells coordinate the activity of separate ion channels that allow electrolytes into the cell. However, a perplexing problem in channel regulation has arisen in the fatal genetic disease cystic fibrosis, which results from the loss of a specific Cl− channel (the CFTR channel) in epithelial cell membranes[1]. Although this defect clearly inhibits the absorption of Na+ in sweat glands[2,3], it is widely accepted that Na+ absorption is abnormally elevated in defective airways in cystic fibrosis[4,5]. The only frequently cited explanation for this hypertransport is that the activity of an epithelial Na+ channel
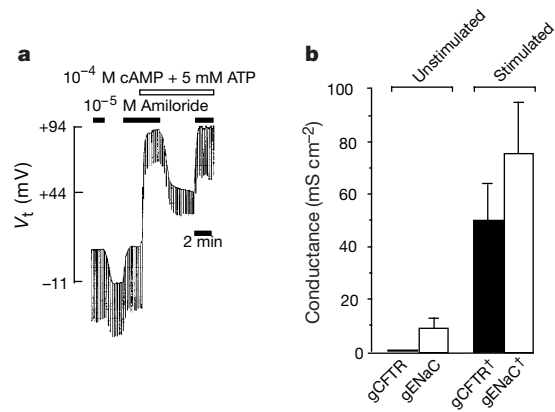
Figure 1 Effect of cAMP and ATP activation of CFTR Cl− conductance (gCFTR) on amiloride-sensitive epithelial Na+ conductance (gENaC). **a**, Diffusion potentials and constant current−pulse potentials across the apical membrane. Without stimulation, CFTR is completely deactivated, but a small stimulation-insensitive, amiloride-sensitive Na+ diffusion potential and gENaC remain. However, stimulation results in a significant increase in both gCFTR and gENaC† (see text). **b**, Mean conductances of gCFTR (filled columns) and gENaC (open columns) measured under baseline conditions (Unstimulated) and after gCFTR when stimulated with 0.1 mM cAMP plus 5 mM ATP (Stimulated) ($P < 0.01$, $n = 15$).

important consequence of nonlinear gravitational processes if the initial conditions are gaussian, and is a potentially powerful signature to exploit in statistical tests of this class of models; see Fig. 1.

The information needed to fully specify a non-gaussian field (or, in a wider context, the information needed to define an image[8]) resides in the complete set of Fourier phases. Unfortunately, relatively little is known about the behaviour of Fourier phases in the nonlinear regime of gravitational clustering[9–14], but it is essential to understand phase correlations in order to design efficient statistical tools for the analysis of clustering data. A first step on the road to a useful quantitative description of phase information is to represent it visually. We do this using colour, as shown in Fig. 2. To view the phase coupling in an N-body simulation, we Fourier-transform the density field; this produces a complex array containing the real (R) and imaginary (I) parts of the transformed 'image', with the pixels in this array labelled by wavenumber $\mathbf{k}$ rather than position $\mathbf{x}$. The phase for each wavenumber, given by $\phi = \arctan(I/R)$, is then represented as a hue for that pixel.

The rich pattern of phase information revealed by this method (see Fig. 3) can be quantified, and related to the gravitational dynamics of its origin. For example, in our analysis of phase coupling[5] we introduced a quantity D_k:

$$D_k \equiv \phi_{k+1} - \phi_k \qquad (4)$$

This quantity measures the difference in phase of modes with neighbouring wavenumbers in one dimension. We refer to D_k as the phase gradient. To apply this idea to a two-dimensional simulation, we simply calculate gradients in the x and y directions independently. Because the difference between two circular random variables is itself a circular random variable, the distribution of D_k should initially be uniform. As the fluctuations evolve waves begin to collapse, spawning higher-frequency modes in phase with the original[15]. These then interact with other waves to produce the non-uniform distribution of D_k seen in Fig. 3.

It is necessary to develop quantitative measures of phase information that can describe the structure displayed in the colour representations. In the beginning, the phases ϕ_k are random and so are the D_k obtained from them. This corresponds to a state of minimal information, or in other words, maximum entropy. As information flows into the phases, the information content must increase and the entropy decrease. This can be quantified by defining an information entropy for the set of phase gradients[5]. We construct a frequency distribution, $f(D)$, of the values of D_k obtained from the whole map. The entropy is then defined as

$$S(D) = - \int f(D) \log[f(D)] \mathrm{d}D \qquad (5)$$

where the integral is taken over all values of D, that is, from 0 to 2π. The use of D, rather than ϕ itself, to define entropy is one way of accounting for the lack of translation invariance of ϕ, a problem that was missed in previous attempts to quantify phase entropy[16]. A uniform distribution of D is a state of maximum entropy (minimum information), corresponding to gaussian initial conditions (random phases). This maximal value of $S_{\max} = \log(2\pi)$ is a characteristic of gaussian fields. As the system evolves, it moves into states of greater information content (that is, lower entropy). The scaling of S with clustering growth displays interesting properties[5], establishing an important link between the spatial pattern and the physical processes driving clustering growth. This phase information is a unique 'fingerprint' of gravitational instability, and it therefore also furnishes statistical tests of the presence of any initial non-gaussianity[17–19]. □

1. Saunders, W. *et al.* The density field of the local Universe. *Nature* **349**, 32–38 (1991).
2. Shectman, S. *et al.* The Las Campanas redshift survey. *Astrophys. J.* **470**, 172–188 (1996).
3. Smoot, G. F. *et al.* Structure in the COBE differential microwave radiometer first-year maps. *Astrophys. J.* **396**, L1–L4 (1992).
4. Peebles, P. J. E. *The Large-scale Structure of the Universe* (Princeton Univ. Press, Princeton, 1980).
5. Chiang, L.-Y. & Coles, P. Phase information and the evolution of cosmological density perturbations. *Mon. Not R. Astron. Soc.* **311**, 809–824 (2000).
6. Guth, A. H. & Pi, S.-Y. Fluctuations in the new inflationary universe. *Phys. Rev. Lett.* **49**, 1110–1113 (1982).
7. Bardeen, J. M., Bond, J. R., Kaiser, N. & Szalay, A. S. The statistics of peaks of Gaussian random fields. *Astrophys. J.* **304**, 15–61 (1986).
8. Oppenheim, A. V. & Lim, J. S. The importance of phase in signals. *Proc. IEEE* **69**, 529–541 (1981).
9. Ryden, B. S. & Gramann, M. Phase shifts in gravitationally evolving density fields. *Astrophys. J.* **383**, L33–L36 (1991).
10. Scherrer, R. J., Melott, A. L. & Shandarin, S. F. A quantitative measure of phase correlations in density fields. *Astrophys. J.* **377**, 29–35 (1991).
11. Soda, J. & Suto, Y. Nonlinear gravitational evolution of phases and amplitudes in one-dimensional cosmological density fields. *Astrophys. J.* **396**, 379–394 (1992).
12. Jain, B. & Bertschinger, E. Self-similar evolution of gravitational clustering: is $n = 1$ special? *Astrophys. J.* **456**, 43–54 (1996).
13. Jain, B. & Bertschinger, E. Self-similar evolution of gravitational clustering: N-body simulations of the $n = -2$ spectrum. *Astrophys. J.* **509**, 517–530 (1998).
14. Thornton, A. L. *Colour Object Recognition Using a Complex Colour Representation and the Frequency Domain.* Thesis, Univ. Reading (1998).
15. Shandarin, S. F. & Zel'dovich, Ya. B. The large-scale structure: turbulence, intermittency, structures in a self-gravitating medium. *Rev. Mod. Phys.* **61**, 185–220 (1989).
16. Polygiannikis, J. M. & Moussas, X. Detection of nonlinear dynamics in solar wind and a comet using phase-correlation measures. *Sol. Phys.* **158**, 159–172 (1995).
17. Ferreira, P. G., Magueijo, J. & Górski, K. M. Evidence for non-Gaussianity in the COBE DMR 4-year sky maps. *Astrophys. J.* **503**, L1–L4 (1998).
18. Pando, J., Valls-Gabaud, D. & Fang, L. Evidence for scale-scale correlations in the cosmic microwave background radiation. *Phys. Rev. Lett.* **81**, 4568–4571 (1998).
19. Bromley, B. C. & Tegmark, M. Is the cosmic microwave background really non-gaussian? *Astrophys. J.* **524**, L79–L82 (1999).
20. Matarrese, S., Verde, L. & Heavens, A. F. Large-scale bias in the universe: bispectrum method. *Mon. Not. R. Astron. Soc.* **290**, 651–662 (1997).
21. Scoccimarro, R., Couchman, H. M. P. & Frieman, J. A. The bispectrum as a signature of gravitational instability in redshift space. *Astrophys. J.* **517**, 531–540 (1999).
22. Verde, L., Wang, L., Heavens, A. F. & Kamionkowski, M. Large-scale structure, the cosmic microwave background, and primordial non-Gaussianity. *Mon. Not. R. Astron. Soc.* **313**, 141–147 (2000).
23. Stirling, A. J. & Peacock, J. A. Power correlations in cosmology: Limits on primordial non-Gaussian density fields. *Mon. Not. R. Astron. Soc.* **283**, L99–L104 (1996).
24. Foley, J. D. & Van Dam, A. *Fundamentals of Interactive Computer Graphics* (Addison-Wesley, Reading, Massachusetts, 1982).
25. Melott, A. L. & Shandarin, S. F. Generation of large-scale cosmological structures by gravitational clustering. *Nature* **346**, 633–635 (1990).
26. Beacom, J. F., Dominik, K. G., Melott, A. L., Perkins, S. P. & Shandarin, S. F. Gravitational clustering in the expanding Universe—controlled high resolution studies in two dimensions. *Astrophys. J.* **372**, 351–363 (1991).

....

Error and attack tolerance of complex networks

Réka Albert, Hawoong Jeong & Albert-László Barabási

Department of Physics, 225 Nieuwland Science Hall, University of Notre Dame, Notre Dame, Indiana 46556, USA

....

Many complex systems display a surprising degree of tolerance against errors. For example, relatively simple organisms grow, persist and reproduce despite drastic pharmaceutical or environmental interventions, an error tolerance attributed to the robustness of the underlying metabolic network[1]. Complex communication networks[2] display a surprising degree of robustness: although key components regularly malfunction, local failures rarely lead to the loss of the global information-carrying ability of the network. The stability of these and other complex systems is often attributed to the redundant wiring of the functional web defined by the systems' components. Here we demonstrate that error tolerance is not shared by all redundant systems: it is displayed only by a class of inhomogeneously wired networks,

called scale-free networks, which include the World-Wide Web[3-5], the Internet[6], social networks[7] and cells[8]. **We find that such networks display an unexpected degree of robustness, the ability of their nodes to communicate being unaffected even by unrealistically high failure rates. However, error tolerance comes at a high price in that these networks are extremely vulnerable to attacks (that is, to the selection and removal of a few nodes that play a vital role in maintaining the network's connectivity). Such error tolerance and attack vulnerability are generic properties of communication networks.**

The increasing availability of topological data on large networks, aided by the computerization of data acquisition, had led to great advances in our understanding of the generic aspects of network structure and development[9-16]. The existing empirical and theoretical results indicate that complex networks can be divided into two major classes based on their connectivity distribution $P(k)$, giving the probability that a node in the network is connected to k other nodes. The first class of networks is characterized by a $P(k)$ that peaks at an average k and decays exponentially for large k. The most investigated examples of such exponential networks are the random graph model of Erdös and Rényi[9,10] and the small-world model of Watts and Strogatz[11], both leading to a fairly homogeneous network, in which each node has approximately the same number of links, $k \simeq k$. In contrast, results on the World-Wide Web (WWW)[3-5], the Internet[6] and other large networks[17-19] indicate that many systems belong to a class of inhomogeneous networks, called scale-free networks, for which $P(k)$ decays as a power-law, that is $P(k) \sim k^{-\gamma}$, free of a characteristic scale. Whereas the probability that a node has a very large number of connections ($k \gg k$) is practically prohibited in exponential networks, highly connected nodes are statistically significant in scale-free networks (Fig. 1).

We start by investigating the robustness of the two basic connectivity distribution models, the Erdös–Rényi (ER) model[9,10] that produces a network with an exponential tail, and the scale-free model[17] with a power-law tail. In the ER model we first define the N nodes, and then connect each pair of nodes with probability p. This algorithm generates a homogeneous network (Fig. 1), whose connectivity follows a Poisson distribution peaked at k and decaying exponentially for $k \gg k$.

The inhomogeneous connectivity distribution of many real networks is reproduced by the scale-free model[17,18] that incorporates two ingredients common to real networks: growth and preferential attachment. The model starts with m_0 nodes. At every time step t a new node is introduced, which is connected to m of the already-existing nodes. The probability Π_i that the new node is connected to node i depends on the connectivity k_i of node i such that $\Pi_i = k_i/\Sigma_j k_j$. For large t the connectivity distribution is a power-law following $P(k) = 2m^2/k^3$.

The interconnectedness of a network is described by its diameter d, defined as the average length of the shortest paths between any two nodes in the network. The diameter characterizes the ability of two nodes to communicate with each other: the smaller d is, the shorter is the expected path between them. Networks with a very large number of nodes can have quite a small diameter; for example, the diameter of the WWW, with over 800 million nodes[20], is around 19 (ref. 3), whereas social networks with over six billion individuals
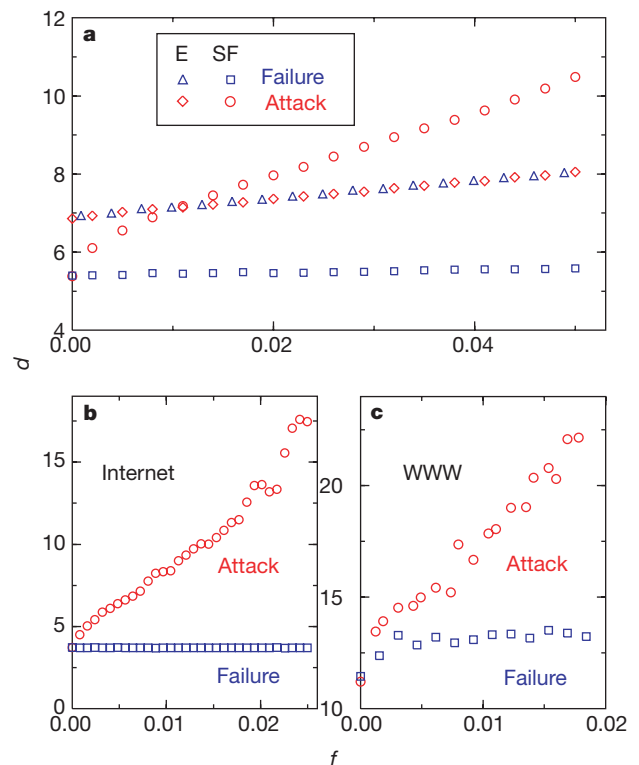

Figure 2 Changes in the diameter d of the network as a function of the fraction f of the removed nodes. **a**, Comparison between the exponential (E) and scale-free (SF) network models, each containing $N = 10,000$ nodes and 20,000 links (that is, $k = 4$). The blue symbols correspond to the diameter of the exponential (triangles) and the scale-free (squares) networks when a fraction f of the nodes are removed randomly (error tolerance). Red symbols show the response of the exponential (diamonds) and the scale-free (circles) networks to attacks, when the most connected nodes are removed. We determined the f dependence of the diameter for different system sizes ($N = 1,000$; 5,000; 20,000) and found that the obtained curves, apart from a logarithmic size correction, overlap with those shown in **a**, indicating that the results are independent of the size of the system. We note that the diameter of the unperturbed ($f = 0$) scale-free network is smaller than that of the exponential network, indicating that scale-free networks use the links available to them more efficiently, generating a more interconnected web. **b**, The changes in the diameter of the Internet under random failures (squares) or attacks (circles). We used the topological map of the Internet, containing 6,209 nodes and 12,200 links ($k = 3.4$), collected by the National Laboratory for Applied Network Research http://moat.nlanr.net/Routing/rawdata/ . **c**, Error (squares) and attack (circles) survivability of the World-Wide Web, measured on a sample containing 325,729 nodes and 1,498,353 links[3], such that $k = 4.59$.

Figure 1 Visual illustration of the difference between an exponential and a scale-free network. **a**, The exponential network is homogeneous: most nodes have approximately the same number of links. **b**, The scale-free network is inhomogeneous: the majority of the nodes have one or two links but a few nodes have a large number of links, guaranteeing that the system is fully connected. Red, the five nodes with the highest number of links; green, their first neighbours. Although in the exponential network only 27% of the nodes are reached by the five most connected nodes, in the scale-free network more than 60% are reached, demonstrating the importance of the connected nodes in the scale-free network Both networks contain 130 nodes and 215 links ($k = 3.3$). The network visualization was done using the Pajek program for large network analysis: http://vlado.fmf.uni-lj.si/pub/networks/pajek/pajekman.htm .

379

are believed to have a diameter of around six[21]. To compare the two network models properly, we generated networks that have the same number of nodes and links, such that $P(k)$ follows a Poisson distribution for the exponential network, and a power law for the scale-free network.

To address the error tolerance of the networks, we study the changes in diameter when a small fraction f of the nodes is removed. The malfunctioning (absence) of any node in general increases the distance between the remaining nodes, as it can eliminate some paths that contribute to the system's interconnectedness. Indeed, for the exponential network the diameter increases monotonically with f (Fig. 2a); thus, despite its redundant wiring (Fig. 1), it is increasingly difficult for the remaining nodes to communicate with each other. This behaviour is rooted in the homogeneity of the network: since all nodes have approximately the same number of links, they all contribute equally to the network's diameter, thus the removal of each node causes the same amount of damage. In contrast, we observe a drastically different and surprising behaviour for the scale-free network (Fig. 2a): the diameter remains unchanged under an increasing level of errors. Thus even when as many as 5% of

the nodes fail, the communication between the remaining nodes in the network is unaffected. This robustness of scale-free networks is rooted in their extremely inhomogeneous connectivity distribution: because the power-law distribution implies that the majority of nodes have only a few links, nodes with small connectivity will be selected with much higher probability. The removal of these 'small' nodes does not alter the path structure of the remaining nodes, and thus has no impact on the overall network topology.

An informed agent that attempts to deliberately damage a network will not eliminate the nodes randomly, but will preferentially target the most connected nodes. To simulate an attack we first remove the most connected node, and continue selecting and removing nodes in decreasing order of their connectivity k. Measuring the diameter of an exponential network under attack, we find that, owing to the homogeneity of the network, there is no substantial difference whether the nodes are selected randomly or in decreasing order of connectivity (Fig. 2a). On the other hand, a drastically different behaviour is observed for scale-free networks. When the most connected nodes are eliminated, the diameter of the scale-free network increases rapidly, doubling its original value if 5% of the nodes are removed. This vulnerability to attacks is rooted in the inhomogeneity of the connectivity distribution: the connectivity is maintained by a few highly connected nodes (Fig. 1b), whose removal drastically alters the network's topology, and
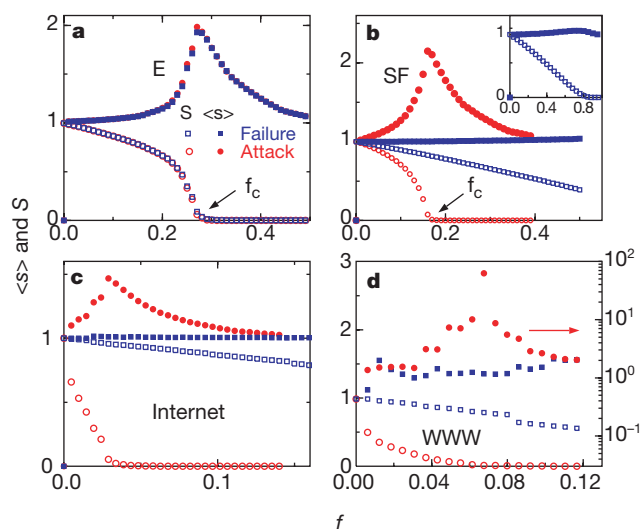
Figure 3 Network fragmentation under random failures and attacks. The relative size of the largest cluster S (open symbols) and the average size of the isolated clusters $\langle s \rangle$ (filled symbols) as a function of the fraction of removed nodes f for the same systems as in Fig. 2. The size S is defined as the fraction of nodes contained in the largest cluster (that is, $S = 1$ for $f = 0$). **a**, Fragmentation of the exponential network under random failures (squares) and attacks (circles). **b**, Fragmentation of the scale-free network under random failures (blue squares) and attacks (red circles). The inset shows the error tolerance curves for the whole range of f, indicating that the main cluster falls apart only after it has been completely deflated. We note that the behaviour of the scale-free network under errors is consistent with an extremely delayed percolation transition: at unrealistically high error rates ($f_{max} \simeq 0.75$) we do observe a very small peak in $\langle s \rangle$ ($\langle s \rangle_{max} \simeq 1.06$) even in the case of random failures, indicating the existence of a critical point. For **a** and **b** we repeated the analysis for systems of sizes $N = 1,000, 5,000$ and $20,000$, finding that the obtained S and $\langle s \rangle$ curves overlap with the one shown here, indicating that the overall clustering scenario and the value of the critical point is independent of the size of the system. **c**, **d**, Fragmentation of the Internet (**c**) and WWW (**d**), using the topological data described in Fig. 2. The symbols are the same as in **b**. $\langle s \rangle$ in **d** in the case of attack is shown on a different scale, drawn in the right side of the frame. Whereas for small f we have $\langle s \rangle \simeq 1.5$, at $f_c^w = 0.067$ the average fragment size abruptly increases, peaking at $\langle s \rangle_{max} \simeq 60$, then decays rapidly. For the attack curve in **d** we ordered the nodes as a function of the number of outgoing links, k_{out}. We note that while the three studied networks, the scale-free model, the Internet and the WWW have different γ, k and clustering coefficient[11], their response to attacks and errors is identical. Indeed, we find that the difference between these quantities changes only f_c and the magnitude of d, S and $\langle s \rangle$, but not the nature of the response of these networks to perturbations.
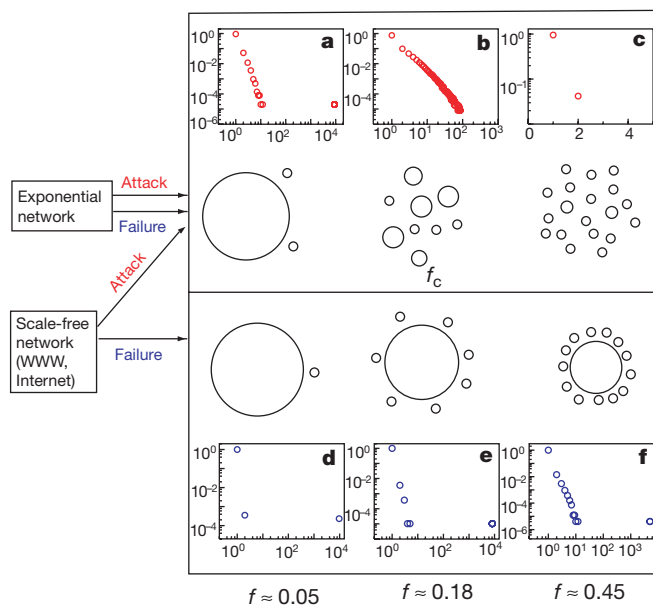
Figure 4 Summary of the response of a network to failures or attacks. **a–f**, The cluster size distribution for various values of f when a scale-free network of parameters given in Fig. 3b is subject to random failures (**a–c**) or attacks (**d–f**). Upper panels, exponential networks under random failures and attacks and scale-free networks under attacks behave similarly. For small f, clusters of different sizes break down, although there is still a large cluster. This is supported by the cluster size distribution: although we see a few fragments of sizes between 1 and 16, there is a large cluster of size 9,000 (the size of the original system being 10,000). At a critical f_c (see Fig. 3) the network breaks into small fragments between sizes 1 and 100 (**b**) and the large cluster disappears. At even higher f (**c**) the clusters are further fragmented into single nodes or clusters of size two. Lower panels, scale-free networks follow a different scenario under random failures: the size of the largest cluster decreases slowly as first single nodes, then small clusters break off. Indeed, at $f = 0.05$ only single and double nodes break off (**d**). At $f = 0.18$, the network is fragmented (**b**) under attack, but under failures the large cluster of size 8,000 coexists with isolated clusters of sizes 1 to 5 (**e**). Even for an unrealistically high error rate of $f = 0.45$ the large cluster persists, the size of the broken-off fragments not exceeding 11 (**f**).

decreases the ability of the remaining nodes to communicate with each other.

When nodes are removed from a network, clusters of nodes whose links to the system disappear may be cut off (fragmented) from the main cluster. To better understand the impact of failures and attacks on the network structure, we next investigate this fragmentation process. We measure the size of the largest cluster, S, shown as a fraction of the total system size, when a fraction f of the nodes are removed either randomly or in an attack mode. We find that for the exponential network, as we increase f, S displays a threshold-like behaviour such that for $f > f_c^e \simeq 0.28$ we have $S \simeq 0$. Similar behaviour is observed when we monitor the average size s of the isolated clusters (that is, all the clusters except the largest one), finding that s increases rapidly until $s \simeq 2$ at f_c^e, after which it decreases to $s = 1$. These results indicate the following breakdown scenario (Fig. 3a). For small f, only single nodes break apart, $s \simeq 1$, but as f increases, the size of the fragments that fall off the main cluster increases, displaying unusual behaviour at f_c^e. At f_c^e the system falls apart; the main cluster breaks into small pieces, leading to $S \simeq 0$, and the size of the fragments, s, peaks. As we continue to remove nodes ($f > f_c^e$), we fragment these isolated clusters, leading to a decreasing s. Because the ER model is equivalent to infinite dimensional percolation[22], the observed threshold behaviour is qualitatively similar to the percolation critical point.

However, the response of a scale-free network to attacks and failures is rather different (Fig. 3b). For random failures no threshold for fragmentation is observed; instead, the size of the largest cluster slowly decreases. The fact that $s \approx 1$ for most f values indicates that the network is deflated by nodes breaking off one by one, the increasing error level leading to the isolation of single nodes only, not clusters of nodes. Thus, in contrast with the catastrophic fragmentation of the exponential network at f_c^e, the scale-free network stays together as a large cluster for very high values of f, providing additional evidence of the topological stability of these networks under random failures. This behaviour is consistent with the existence of an extremely delayed critical point (Fig. 3) where the network falls apart only after the main cluster has been completely deflated. On the other hand, the response to attack of the scale-free network is similar (but swifter) to the response to attack and failure of the exponential network (Fig. 3b): at a critical threshold $f_c^{sf} \simeq 0.18$, smaller than the value $f_c^e \simeq 0.28$ observed for the exponential network, the system breaks apart, forming many isolated clusters (Fig. 4).

Although great efforts are being made to design error-tolerant and low-yield components for communication systems, little is known about the effect of errors and attacks on the large-scale connectivity of the network. Next, we investigate the error and attack tolerance of two networks of increasing economic and strategic importance: the Internet and the WWW.

Faloutsos et al.[6] investigated the topological properties of the Internet at the router and inter-domain level, finding that the connectivity distribution follows a power-law, $P(k) \sim k^{-2.48}$. Consequently, we expect that it should display the error tolerance and attack vulnerability predicted by our study. To test this, we used the latest survey of the Internet topology, giving the network at the inter-domain (autonomous system) level. Indeed, we find that the diameter of the Internet is unaffected by the random removal of as high as 2.5% of the nodes (an order of magnitude larger than the failure rate (0.33%) of the Internet routers[23]), whereas if the same percentage of the most connected nodes are eliminated (attack), d more than triples (Fig. 2b). Similarly, the large connected cluster persists for high rates of random node removal, but if nodes are removed in the attack mode, the size of the fragments that break off increases rapidly, the critical point appearing at $f_c^I \simeq 0.03$ (Fig. 3b).

The WWW forms a huge directed graph whose nodes are documents and edges are the URL hyperlinks that point from one document to another, its topology determining the search engines' ability to locate information on it. The WWW is also a scale-free network: the probabilities $P_{out}(k)$ and $P_{in}(k)$ that a document has k outgoing and incoming links follow a power-law over several orders of magnitude, that is, $P(k) \sim k^{-\gamma}$, with $\gamma_{in} = 2.1$ and $\gamma_{out} = 2.45^{3,4,24}$. Since no complete topological map of the WWW is available, we limited our study to a subset of the web containing 325,729 nodes and 1,469,680 links ($\bar{k} = 4.59$) (ref. 3). Despite the directedness of the links, the response of the system is similar to the undirected networks we investigated earlier: after a slight initial increase, d remains constant in the case of random failures and increases for attacks (Fig. 2c). The network survives as a large cluster under high rates of failure, but the behaviour of s indicates that under attack the system abruptly falls apart at $f_c^w = 0.067$ (Fig. 3c).

In summary, we find that scale-free networks display a surprisingly high degree of tolerance against random failures, a property not shared by their exponential counterparts. This robustness is probably the basis of the error tolerance of many complex systems, ranging from cells[8] to distributed communication systems. It also explains why, despite frequent router problems[23], we rarely experience global network outages or, despite the temporary unavailability of many web pages, our ability to surf and locate information on the web is unaffected. However, the error tolerance comes at the expense of attack survivability: the diameter of these networks increases rapidly and they break into many isolated fragments when the most connected nodes are targeted. Such decreased attack survivability is useful for drug design[8], but it is less encouraging for communication systems, such as the Internet or the WWW. Although it is generally thought that attacks on networks with distributed resource management are less successful, our results indicate otherwise. The topological weaknesses of the current communication networks, rooted in their inhomogeneous connectivity distribution, seriously reduce their attack survivability. This could be exploited by those seeking to damage these systems. □

1. Hartwell, L. H., Hopfield, J. J., Leibler, S. & Murray, A. W. From molecular to modular cell biology. *Nature* **402,** 47–52 (1999).
2. Claffy, K., Monk, T. E. *et al.* Internet tomography. *Nature Web Matters* [online] (7 Jan. 99) http://helix.nature.com/webmatters/tomog/tomog.html (1999).
3. Albert, R., Jeong, H. & Barabási, A.-L. Diameter of the World-Wide Web. *Nature* **401,** 130–131 (1999).
4. Kumar, R., Raghavan, P., Rajalopagan, S. & Tomkins, A. in *Proc. 9th ACM Symp. on Principles of Database Systems* 1–10 (Association for Computing Machinery, New York, 2000).
5. Huberman, B. A. & Adamic, L. A. Growth dynamics of the World-Wide Web. *Nature* **401,** 131 (1999).
6. Faloutsos, M., Faloutsos, P. & Faloutsos, C. On power-law relationships of the internet topology, ACM SIGCOMM '99. *Comput. Commun. Rev.* **29,** 251–263 (1999).
7. Wasserman, S. & Faust, K. *Social Network Analysis* (Cambridge Univ. Press, Cambridge, 1994).
8. Jeong, H., Tombor, B., Albert, R., Oltvai, Z. & Barabási, A.-L. The large-scale organization of metabolic networks. *Nature* (in the press).
9. Erdös, P. & Rényi, A. On the evolution of random graphs. *Publ. Math. Inst. Hung. Acad. Sci.* **5,** 17–60 (1960).
10. Bollobás, B. *Random Graphs* (Academic, London, 1985).
11. Watts, D. J. & Strogatz, S. H. Collective dynamics of 'small-world' networks. *Nature* **393,** 440–442 (1998).
12. Zegura, E. W., Calvert, K. L. & Donahoo, M. J. A quantitative comparison of graph-based models for internet topology. *IEEE/ACM Trans. Network.* **5,** 770–787 (1997).
13. Williams, R. J. & Martinez, N. D. Simple rules yield complex food webs. *Nature* **404,** 180–183 (2000).
14. Maritan, A., Colaiori, F., Flammini, A., Cieplak, M. & Banavar, J. Universality classes of optimal channel networks. *Science* **272,** 984–986 (1996).
15. Banavar, J. R., Maritan, A. & Rinaldo, A. Size and form in efficient transportation networks. *Nature* **399,** 130–132 (1999).
16. Barthélémy, M. & Amaral, L. A. N. Small-world networks: evidence for a crossover picture. *Phys. Rev. Lett.* **82,** 3180–3183 (1999).
17. Barabási, A.-L. & Albert, R. Emergence of scaling in random networks. *Science* **286,** 509–511 (1999).
18. Barabási, A.-L., Albert, R. & Jeong, H. Mean-field theory for scale-free random networks. *Physica A* **272,** 173–187 (1999).
19. Redner, S. How popular is your paper? An empirical study of the citation distribution. *Euro. Phys. J. B* **4,** 131–134 (1998).
20. Lawrence, S. & Giles, C. L. Accessibility of information on the web. *Nature* **400,** 107–109 (1999).
21. Milgram, S. The small-world problem. *Psychol. Today* **2,** 60–67 (1967).
22. Bunde, A. & Havlin, S. (eds) *Fractals and Disordered Systems* (Springer, New York, 1996).
23. Paxson, V. End-to-end routing behavior in the internet. *IEEE/ACM Trans. Network.* **5,** 601–618 (1997).
24. Adamic, L. A. The small world web. *Lect. Notes Comput. Sci.* **1696,** 443–452 (1999).

....

Controlled surface charging as a depth-profiling probe for mesoscopic layers

Ilanit Doron-Mor*, Anat Hatzor*, Alexander Vaskevich*, Tamar van der Boom-Moav†, Abraham Shanzer†, Israel Rubinstein* & Hagai Cohen‡

*Department of Materials and Interfaces, †Department of Organic Chemistry, ‡Department of Chemical Services, Weizmann Institute of Science, Rehovot 76100, Israel

....

Probing the structure of material layers just a few nanometres thick requires analytical techniques with high depth sensitivity. X-ray photoelectron spectroscopy[1] (XPS) provides one such method, but obtaining vertically resolved structural information from the raw data is not straightforward. There are several XPS depth-profiling methods, including ion etching[2], angle-resolved XPS (ref. 2) and Tougaard's approach[3], but all suffer various limitations[2–5]. Here we report a simple, non-destructive XPS depth-profiling method that yields accurate depth information with nanometre resolution. We demonstrate the technique using self-assembled multilayers on gold surfaces; the former contain 'marker' monolayers that have been inserted at predetermined depths. A controllable potential gradient is established vertically through the sample by charging the surface of the dielectric overlayer with an electron flood gun. The local potential is probed by measuring XPS line shifts, which correlate directly with the vertical position of atoms. We term the method 'controlled surface charging', and expect it to be generally applicable to a large variety of mesoscopic heterostructures.

Charging is commonly considered an experimental obstacle to accurate determination of binding energies in XPS measurements of poorly conducting surfaces[6]. To compensate the extra positive charge (a natural consequence of photoelectron emission) and to stabilize the energy scale on a reasonably correct value, an electron flood gun is routinely used, creating a generally uniform potential across the studied volume. This, however, is often impossible with systems comprising components that differ in electrical conductivity[7–9]. In such cases, chemical information may be smeared due to XPS line shifts that follow local potential variations. On the other hand, this very effect can be used to gain structural information[10–12]. We have shown recently that surface charging can be used to analyse self-assembled monolayers on heterogeneous substrates, providing lateral resolution on a scale given by the substrate structural variations—that is, much smaller than the probe size[13]. Here we show that controlled surface charging (CSC) can be applied to obtain nanometre-scale depth resolution in laterally homogeneous structures.

Well-defined correlation between the local potential and the vertical (depth) axis can be achieved in some systems; for example, those consisting of an insulating overlayer on a metallic (grounded) substrate, where the overlayer is laterally uniform. We use such a system in the work reported here. In the present application the flood electron gun is not used for charge neutralization, but rather is operated at a considerably higher flux of electrons; this creates a dynamic balance between charge generation and discharge rates, which is controlled by variation of the flood-gun parameters (that is, electron flux and kinetic energy). Evidently, the extra negative charge is accumulated on the film surface, and a dynamic steady state is reached where the charge leakage to the grounded substrate is balanced by the net incoming flux. With the systems studied here, essentially no space charge is developed within the dielectric film. The resultant vertical field is therefore constant, such that the local potential, correlated directly with XPS line shifts, varies linearly with the depth scale (z), unfolding the spectrum with respect to the vertical scale. The steady-state situation, with a surface charge density σ and an overlayer dielectric constant ϵ, is thus modelled by a parallel-plate capacitor, where the local potential ϕ between the plates is given by equation (1) (σ is determined by the overlayer resistivity and the flood-gun operating conditions).

$$\phi(z) = 4\pi\sigma z/\epsilon \qquad (1)$$

The studied substrates comprised a 100-nm {111} textured gold layer, evaporated on a highly polished doped Si(111) wafer[14]. Metal–organic coordinated multilayers were constructed layer-by-layer on the gold surface as previously described[14]. The base layer was a disulphide-bishydroxamate molecule (compound **1** in Fig. 1d)[15]. Two different bifunctional ligand repeat units were used, a tetrahydroxamate (**2**, Fig. 1d)[14] and a diphosphonate (**3**, Fig. 1d)[16–18], connected by three different tetravalent metal ions: Zr^{4+}, Ce^{4+} or Hf^{4+}.

XPS measurements were performed on a Kratos Analytical AXIS-HS Instrument, using a monochromatized Al (Kα) source ($h\nu = 1,486.6$ eV) at a relatively low power[13]. The flood gun was used under varying conditions, of which four are presented here (see Fig. 2 legend). Accurate determination of line shifts was achieved by graphically shifting lines until a statistically optimal match was obtained. This procedure, correlating the full line shape (100–200 data points), allowed excellent accuracy ($\sim$0.03 eV) in the determination of energy shifts, much beyond the experimental energy resolution (that is, source and bare line widths). In cases where the external charging induced line-shape changes, larger uncertainties were considered. The shifts were translated to potential differences relative to the gold by subtracting the corresponding gold line shifts. Special effort was made to determine time periods characteristic of the stabilization of local potentials, which were generally longer for the lower flood-gun flux. This was of particular importance in view of beam-induced damage[5], which was observed after an hour or more and found to slightly distort the CSC behaviour. The latter will be discussed elsewhere.

For a general demonstration of CSC, two sets of multilayers with varying thicknesses (2 to 10 layers) were constructed (Fig. 1a), using the tetrahydroxamate ligand **2**. Each set was assembled with a different binding ion, that is, Zr(IV) or Ce(IV), respectively. The spectral response to the flood-gun flux is shown in Fig. 2a. The various surface elements manifest energy shifts and line-shape changes, both associated with the development of vertical potential gradients: the Au 4f line shifts by a very small amount, attributed to the finite (sample-dependent) conductivity of the silicon substrate. All other overlayer elements exhibit much larger shifts, with differences correlated with their spatial (depth) distribution. The energy shifts and line shapes of elements not shown in Fig. 2 (N, O) are fully consistent with the model.

In these two sets of samples, all the overlayer elements (except sulphur) are distributed along the vertical scale. This complicates the derivation of local potentials in general, and specifically the overall potential difference, V_0, developed across the entire overlayer. (V_0 here is relative to the 'gun-off' situation.) Yet an approximate analysis can be performed by curve-fitting the metal ion lines to sets of discrete signals, corresponding to ion interlayers at